



Nunez, P., Richter, M., Piercy, B., Roske, C., Caban-Acevedo, M., Losego, M., Konezny, S., Fermin, D., Hu, S., Brunschwig, B., & Lewis, N. (2019). Characterization of Electronic Transport through Amorphous TiO₂ Produced by Atomic-Layer Deposition. *Journal of Physical Chemistry C*, 123(33), 20116 - 20129.
<https://doi.org/10.1021/acs.jpcc.9b04434>

Peer reviewed version

Link to published version (if available):
[10.1021/acs.jpcc.9b04434](https://doi.org/10.1021/acs.jpcc.9b04434)

[Link to publication record in Explore Bristol Research](#)
PDF-document

This is the author accepted manuscript (AAM). The final published version (version of record) is available online via ACS at <https://pubs.acs.org/doi/10.1021/acs.jpcc.9b04434> . Please refer to any applicable terms of use of the publisher.

University of Bristol - Explore Bristol Research

General rights

This document is made available in accordance with publisher policies. Please cite only the published version using the reference above. Full terms of use are available:
<http://www.bristol.ac.uk/red/research-policy/pure/user-guides/ebr-terms/>

This document is confidential and is proprietary to the American Chemical Society and its authors. Do not copy or disclose without written permission. If you have received this item in error, notify the sender and delete all copies.

Characterization of Electronic Transport through Amorphous TiO₂ Produced by Atomic-Layer Deposition

Journal:	<i>The Journal of Physical Chemistry</i>
Manuscript ID	jp-2019-04434d
Manuscript Type:	Article
Date Submitted by the Author:	09-May-2019
Complete List of Authors:	Nunez, Paul; California Institute of Technology Division of Chemistry and Chemical Engineering Richter, Matthias; California Institute of Technology, Division of Chemistry and Chemical Engineering Piercy, Brandon; Georgia Institute of Technology Roske, Christopher; California Institute of Technology, Chemistry and Chemical Engineering Cabán-Acevedo, Miguel; California Institute of Technology, Division of Chemistry and Chemical Engineering Losego, Mark; Georgia Institute of Technology, Materials Science and Engineering Konezny, Steven; Yale University, Department of Chemistry Fermin, David; University of Bristol, School of Chemistry Hu, Shu; Yale University, Brunschwig, Bruce; California Institute of Technology, Beckman Institute Lewis, Nathan; California Institute of Technology, Chemistry and Chemical Engineering

SCHOLARONE™
Manuscripts

Characterization of Electronic Transport through Amorphous TiO₂ Produced by Atomic-Layer Deposition

Paul Nunez,[†] Matthias H. Richter,[†] Brandon D. Piercy,[‡] Christopher W. Roske,[†] Miguel Cabán-Acevedo,[†] Mark D. Losego,[‡] Steven J. Konezny,^{§,||} David J. Fermin,[⊥] Shu Hu,^{*,§,#} Bruce S. Brunschwig,[∇] and Nathan S. Lewis^{*,†,∇}

[†] Division of Chemistry and Chemical Engineering, California Institute of Technology, Pasadena, California 91125, USA.

[‡] School of Materials Science and Engineering, Georgia Institute of Technology, Atlanta, GA 30332, USA.

[§] Energy Sciences Institute, Yale West Campus, West Haven, CT 06516, USA.

^{||} Department of Chemistry, Yale University, 225 Prospect Street, P.O. Box 208107, New Haven, Connecticut, 06520-8107, USA.

[⊥] School of Chemistry, University of Bristol, Cantock's Close, Bristol BS8 1TS, United Kingdom.

[#] Department of Chemical and Environmental Engineering, School of Engineering and Applied Sciences, Yale University, New Haven, CT 06520, USA.

[∇] Beckman Institute and Molecular Materials Research Center, California Institute of Technology, Pasadena, CA 91125, USA.

Keywords:

Amorphous, Titanium dioxide, atomic-layer deposition, silicon, defect states, conduction mechanism, Ti³⁺

ABSTRACT:

The electrical transport in amorphous titanium dioxide (*a*-TiO₂) thin films deposited by atomic-layer deposition (ALD), and across heterojunctions of p⁺-Si|*a*-TiO₂|metal substrates that had various top metal contacts, has been characterized by AC conductivity, temperature-dependent DC conductivity, space-charge-limited current (SCLC) spectroscopy, electron paramagnetic resonance (EPR), X-ray photoelectron spectroscopy (XPS), and current density versus voltage (*J-V*) characteristics. Amorphous TiO₂ films were fabricated using either tetrakis(dimethylamido)-titanium (TDMAT) with a substrate temperature of 150 °C or TiCl₄ with a substrate temperature of 50, 100, or 150 °C. EPR spectroscopy of the films showed that the Ti³⁺ concentration varied with the deposition conditions, and increases in the concentration of Ti³⁺ in the films correlated with increases in film conductivity. Valence-band spectra for the *a*-TiO₂ films exhibited a defect-state peak below the conduction-band minimum (CBM), and increases in the intensity of this peak correlated with increases in the Ti³⁺ concentration measured by EPR as well as with increases in film conductivity. The temperature dependent conduction data showed Arrhenius behavior at room temperature with an activation energy that decreased with decreasing temperature, suggesting that conduction did not occur primarily through either the valence or conduction bands. The data from all of the measurements are consistent with a Ti³⁺ defect-mediated transport mode involving a hopping mechanism with a defect density of 10¹⁹ cm⁻³, a 0.83 eV wide defect-band centered 1.47 eV below the CBM, and a free-electron concentration of 10¹⁶ cm⁻³. The data are consistent with substantial room-temperature anodic conductivity resulting from introduction of defect states during the ALD

1
2
3 fabrication process as opposed charge transport intrinsically associated with the conduction band
4
5 of TiO₂.
6
7
8
9
10
11
12
13
14
15
16
17
18
19
20
21
22
23
24
25
26
27
28
29
30
31
32
33
34
35
36
37
38
39
40
41
42
43
44
45
46
47
48
49
50
51
52
53
54
55
56
57
58
59
60

I. INTRODUCTION

Water oxidation to evolve $O_2(g)$ is a key process in the (photo-)electrochemical production of carbon-neutral fuels. Semiconductors with band gaps, E_g , that allow substantial absorption of sunlight ($E_g < 2$ eV) typically corrode, either through dissolution or through the formation of an insoluble insulating surface oxide, when placed in contact with an aqueous electrolyte and poised at a potential sufficiently positive to drive the water-oxidation half-reaction.¹ Such corrosion has impeded the development of fully integrated solar fuels devices that involve immersion of semiconductors in an electrolyte,² and is especially rapid in the strongly acidic or strongly alkaline electrolytes that are compatible with efficient operation of electrochemical cells and with existing ion-exchange membranes.³ Coating such semiconductors with films that combine transparent, conductive oxides with active catalysts for the oxygen-evolution reaction (OER) has been shown to extend the lifetime of semiconductor anodes in aqueous electrolytes from seconds to hours or months,⁴⁻¹³ depending on the specific materials and test conditions.

Coatings of amorphous TiO_2 (*a*- TiO_2) supporting a Ni OER catalyst provide stability against corrosion of technologically important n-type semiconductors including n-Si, n-GaAs, and n-CdTe, in strongly alkaline electrolytes under water-oxidation conditions.^{4, 14} The relative alignment between the valence-band maximum (VBM) of these n-type materials and the VBM of n-type TiO_2 ($E_g \sim 3.3$ eV) predicts an ~ 2 eV barrier to the transport of holes from the smaller-band-gap material into the *a*- TiO_2 .¹⁵ Nevertheless, these heterojunction devices support high anodic current densities (> 100 mA cm^{-2}).^{4, 14} Conduction through the *a*- TiO_2 films has been shown to be essentially independent of the film thickness, with high conductance observed for films as thick as 143 nm; however, the interfacial conductance is strongly dependent on the top

1
2
3 contact. Specifically, to drive anodic current densities of $50 - 120 \text{ mA cm}^{-2}$, an Ir top contact
4 increased the voltage required by $\sim 400 \text{ mV}$ relative to devices with Ni top contacts.⁴ X-ray
5 photoelectron spectroscopic (XPS) data indicate a band alignment that produces rectifying
6 behavior for $a\text{-TiO}_2$ interfaces with n-Si and $n^+\text{-Si}$ surfaces, and an ohmic contact between $a\text{-}$
7 TiO_2 and $p^+\text{-Si}$.¹⁶ Ambient-pressure XPS (AP-XPS) data of $p^+\text{-Si}|a\text{-TiO}_2$ electrodes under
8 potential control indicate that the addition of Ni to the surface of $a\text{-TiO}_2$ changes the electrical
9 behavior of the $a\text{-TiO}_2|\text{liquid}$ junction. Bare $a\text{-TiO}_2$ electrodes in contact with solution are
10 ‘rectifying’ for the oxidation of water or $\text{Fe}(\text{CN})_6^{4-}$. This rectifying behavior is also observed for
11 contact between a Hg droplet and bare $a\text{-TiO}_2$. The addition of a Ni layer to the $a\text{-TiO}_2$ makes
12 the junction ohmic, removing a large energetic barrier to conduction across the $a\text{-TiO}_2$.¹⁷

13
14
15
16
17
18
19
20
21
22
23
24
25
26
27
28
29
30
31
32
33
34
35
36
37
38
39
40
41
42
43
44
45
46
47
48
49
50
51
52
53
54
55
56
57
58
59
60
These data provide a detailed picture of the energetics at $n\text{-Si}|a\text{-TiO}_2|\text{Ni}|1.0 \text{ M KOH}(\text{aq})$
interfaces. However, the mechanism of conduction across the $n\text{-Si}|a\text{-TiO}_2|\text{Ni}$ junctions, despite
the unfavorable band alignment energetics, remains to be elucidated. XPS valence-band data
show a weak peak $\sim 2 \text{ eV}$ above the valence-band maximum, suggesting the possibility of
defect-based transport.⁴ However, subsequent studies have observed anodic conduction by TiO_2
films synthesized using various techniques, including crystalline films, and did not yield a
dependence of conduction on defect states.¹⁸ For TiO_2 -coated photocathodes, conduction occurs
via electron transport in the TiO_2 conduction band.¹⁹⁻²¹ Such electron transport mediated by the
conduction band has been hypothesized to be a generic mechanism applicable to photoanodes,
with TiO_2 operating as an ohmic contact to the underlying n-type semiconductor, with electrons
being transported from solution via the TiO_2 conduction band recombining with holes at the
semiconductor| TiO_2 junction.²²

1
2
3 Ti^{3+} states (observable by electron-paramagnetic resonance, EPR and XPS valence band
4 spectra) play a large role in the conductivity, light absorption, and many other properties of
5 TiO_2 .²³⁻³⁰ The mechanism of facile hole conduction through *a*- TiO_2 , despite the 3.0 eV band gap
6 and unfavorable band edge energetics for either electron or hole conduction from small band gap
7 inorganic semiconductors has not yet been elucidated. A greater understanding of the transport
8 mechanism would provide insight into the utility and mechanism underpinning the use of ALD
9 *a*- TiO_2 as a protection layer for a wide variety of photoanodes.
10
11
12
13
14
15
16
17
18

19 We describe herein a detailed investigation of conduction across $\text{p}^+ \text{-Si} | a\text{-TiO}_2$ junctions,
20 including temperature-dependent DC conductivity, AC conductivity, space-charge-limited
21 current spectroscopy, electron paramagnetic resonance (EPR) and X-ray photoelectron
22 spectroscopy (XPS). The experiments were designed to elucidate the mechanism of anodic
23 conduction in *a*- TiO_2 layers as well as the factors that control the observed conductivity as the
24 metal contact to the *a*- TiO_2 layer is varied. We consequently have explored the role of defect
25 states in conduction across *a*- TiO_2 films fabricated by a variety of methods, as well as the
26 importance of the energy-band positions of the Si and the top contact relative to the TiO_2 band
27 positions. We have moreover applied the information gained from these studies to aid in the
28 design of stable $\text{Si} | a\text{-TiO}_2$ photoanodes with high fill factors for solar-driven water oxidation in
29 contact with acidic aqueous electrolytes.
30
31
32
33
34
35
36
37
38
39
40
41
42
43
44

45 **II. EXPERIMENTAL**

46 **A. Sample Preparation**

47 *Materials and Chemicals*

48
49 Water with a resistivity, ρ , $> 18 \text{ M}\Omega \cdot \text{cm}$ was obtained from a Barnsted Millipore
50 purification system and was used throughout. All chemicals, including sulfuric acid (99.999%,
51
52
53
54
55
56
57
58
59
60

1
2
3 Sigma-Aldrich and ~ 18 M, ACS Reagent Grade, J.T. Baker), hydrogen peroxide (~ 30%, ~ 13
4 M, VWR), hydrochloric acid (ACS Grade, VWR), and buffered HF (aq) (semiconductor-grade,
5 Transene), were used as received, unless otherwise noted. Two types of crystalline, single-side
6 polished, Si substrates were used: p⁺-Si(100) (Boron-doped, $\rho < 0.002 \Omega \cdot \text{cm}$, Addison
7 Engineering) and n-Si(100) (Phosphorus-doped, $\rho = 2 - 3 \Omega \cdot \text{cm}$, Addison Engineering).
8
9

15 *Preparation of Substrates*

17 The Si wafers were cleaned using an RCA SC-1 procedure that consisted of a 10 min
18 soak in a 3:1 (by volume) solution made from 3 parts H₂SO₄ (aq) (~ 18 M) and 1 part H₂O₂(aq)
19 (~ 13 M). The samples were then briefly etched in a solution of buffered HF(aq) (Transene). The
20 Si samples were cleaned using an RCA SC-2 procedure by soaking the samples for 10 min at 75
21 °C in a 5:1:1 (by volume) solution of H₂O, HCl(aq) (~ 11 M), and H₂O₂(aq) (~ 13 M). The RCA
22 SC-2 procedure left a thin passivating oxide layer on the Si surface.
23
24
25
26
27
28
29

31 *Atomic-Layer Deposition (ALD) of TiO₂ Thin Films*

33 TiO₂ films were grown using two different precursors, tetrakis(dimethylamido)-titanium
34 (TDMAT), and TiCl₄. For TiO₂ films prepared from the TDMAT precursor, a Cambridge
35 Nanotech S200 or Fiji F200 ALD system was used to deposit TiO₂ films onto Si wafers or onto
36 Pyrex micro cover glass slides (VWR). The defect characteristics of TiO₂ were similar for films
37 prepared from either reactor. Each ALD cycle consisted of a 0.10 s exposure to TDMAT (Sigma-
38 Aldrich, 99.999%), a N₂(g) (Airgas, 99.999%) purge, a 0.015 s exposure to H₂O, and a final
39 N₂(g) purge. Research grade 20 sccm N₂(g) was used for the N₂(g) purges, and each N₂(g) purge
40 was 15 s in duration. During deposition, the substrate and the TDMAT precursor were heated to
41 150 °C and 75 °C, respectively, while the H₂O remained at room temperature. Most samples
42 were prepared with 1500 cycles, giving a nominal thickness of 68 nm. The thickness was chosen
43
44
45
46
47
48
49
50
51
52
53
54
55
56
57
58
59
60

1
2
3 to be consistent with previous work. At this thickness, the a -TiO₂ minimizes the reflection as a
4 single-layer anti-reflection coating while still providing facile electronic conduction and
5
6 corrosion protection of the underlying photoanode.³¹
7
8

9
10 TiO₂ films from the TiCl₄ precursor were deposited onto p⁺-Si substrates in a hot-wall,
11 flow-tube reactor with custom-designed sequencing software.³² The precursor-gas lines were
12 maintained at 110 °C whereas the precursor was maintained at room temperature. Each ALD
13 cycle consisted of a 0.20 s exposure to TiCl₄ (Strem, 99%), a 45 s N₂(g) purge, a 0.10 s exposure
14 to H₂O, and a final 30 s N₂(g) purge and the N₂(g) flow rate was 150 sccm. Films were
15 deposited to a predetermined thickness of ~ 60 nm at chamber temperatures of 50, 100, or 150
16 °C. The film thickness and refractive index were measured via spectroscopic ellipsometry (J.A.
17 Woollam Co., alpha-SE) and were fit to a Cauchy model.
18
19
20
21
22
23
24
25
26
27

28 *Electron-Beam Metal Deposition*

29
30
31 Samples were patterned via optical lithography, mounted with double-sided carbon tape,
32 and pumped down to a base pressure of <10⁻⁵ Torr in an electron-beam evaporator system
33 (Ångstrom Engineering Inc.). Ti, Mg, Ni, Au, Ir, Pt and Pd were evaporated from source metals
34 that were at least 4N purity. Deposition rates ranged from 0.020 to 0.080 nm s⁻¹, as monitored by
35 a quartz-crystal microbalance. Deposition was stopped when the film thickness exceeded ~ 35
36 nm.
37
38
39
40
41
42
43

44 *Electrode Fabrication*

45
46
47 Electrodes were fabricated by using a scribe to cleave the e-beam deposited samples into ~
48 0.1 cm² pieces. The samples were patterned into isolated pads for solid-state measurements or
49 into islands for electrochemical measurements. A positive photoresist, S1813 (Shipley), was
50 patterned, metal pads or islands deposited, and then the photoresist was removed by gently
51
52
53
54
55
56
57
58
59
60

1
2
3 sonicating in acetone for ~ 1 min to leave the desired pattern. Ohmic contact was made by
4 scratching the back of the p^+ -Si or n-Si sample with an In-Ga eutectic (Alfa-Aesar, 99.999%),
5
6 and the back contact to the sample was affixed to a Cu wire with double-sided Cu tape. The Cu
7
8 wire was threaded through a glass tube (Corning Incorporation, Pyrex tubing, 7740 glass), and
9
10 all but the front of the sample was encapsulated with Loctite epoxy (Hysol 9462). After curing
11
12 overnight, the electrode was scanned with an Epson scanner (V370) and analyzed with ImageJ
13
14 software, to determine the area of the exposed region, which was $\sim 0.1 \text{ cm}^2$.
15
16
17
18

19 **B. Conductivity Measurements**

20
21 Current density versus voltage (J - V) data were collected on solid-state samples that had
22
23 various combinations of metal contacts on degenerately boron-doped p^+ -Si substrates coated
24
25 with the α -TiO₂. The electrical data were collected using a Bio-Logic SP-200 potentiostat in a
26
27 two-electrode setup with the working electrode lead connected to the bottom contact (Si back-
28
29 side) and the counter and reference electrode leads connected to the top contact (metal pad). For
30
31 electrical contact, In-Ga eutectic was scratched onto the back of the Si as well as onto the top
32
33 side of the double-sided Cu tape that had been affixed to a glass slide for structural support. J - V
34
35 data were collected at 100 mV s^{-1} , starting at an applied bias of 0 V versus the counter electrode.
36
37
38
39

40 *Temperature-Dependent Conductivity*

41
42 The substrates for the measurements were p^+ -Si wafers coated with 1500 cycles (~ 68
43
44 nm) of ALD α -TiO₂ that was then patterned with Ni islands. During the variable temperature
45
46 measurement, the samples were loaded into a Janis CCS-100/204N cryostat, and J - V data were
47
48 obtained from 10 to 310 K using an Agilent B1500A semiconductor-device analyzer with
49
50 medium-power source-measurement modules as well as atto-sense and switch units for high-
51
52
53
54
55
56
57
58
59
60

1
2
3 resolution current sensing. The conductivity was obtained by fitting the measured resistance data
4
5 to a computational model using the AC/DC module in COMSOL Multiphysics software.
6

7
8 For resistance measurements from 180 K to 300 K, the samples were loaded into another
9
10 cryostat. In both temperature-dependent measurements, the temperature of the sample was
11
12 controlled using a Lake Shore auto-tuning temperature controller with a Si diode temperature
13
14 sensor placed in thermal contact with the sample.
15

16
17 *Potential-Dependent Conductance Measurements on Electrochemical Field-Effect Transistors*
18
19 *(EC-FET)*
20

21
22 The conductance of α -TiO₂ films in contact with an electrolyte solution was measured
23
24 with interdigitated electrodes (IDE) in an electrochemical field-effect-transistor configuration
25
26 (EC-FET).³³⁻³⁴ The substrates for the measurements were clean glass microscope slides that had
27
28 been lithographically patterned with 224 interdigitated Ti fingers of 20 $\mu\text{m} \times 2 \text{ mm} \times 100 \text{ nm}$
29
30 (width \times length \times thickness). Alternate fingers were spaced 20 μm apart from one another. The
31
32 substrate had 1500 cycles ($\sim 68 \text{ nm}$) of α -TiO₂ deposited via ALD. The front contacts were kept
33
34 free of deposited material by use of a glass slide as a physical mask. The conductance of the α -
35
36 TiO₂ in contact with 1.0 M H₂SO₄(aq) was measured using a BioLogic SP-300 bipotentiostat that
37
38 allowed control of the potential of each electrode (channels) of the IDE array independently with
39
40 respect to the reference electrode in the solution. Both channels were set to the desired gate
41
42 potential (V_{gate}), and the capacitance current was allowed to decay for 30 s, to establish the
43
44 electron occupancy in the film and to set the potential of the film relative to the reference
45
46 potential. The potential of channel 2 was then offset by $\pm 25 \text{ mV}$ with respect to channel 1, and
47
48 the source-drain potential (V_{SD}) was varied in 10 mV increments. Under the conditions
49
50 investigated, the source-drain current (I_{SD}) was proportional to V_{SD} , allowing an estimate of the
51
52
53
54
55
56
57
58
59
60

1
2
3 film conductance as a function of V_{gate} . V_{gate} was varied across the potential range between the
4
5 onset of accumulation and deep depletion. The film conductivity was calculated using an IDE
6
7 cell constant, K_{IDE} , of 0.045 cm^{-1} , which was estimated from the geometry of the IDE³⁵ using eq
8
9
10 1:

$$K_{\text{ide}} = \frac{2 \left(\frac{s}{w} \right)^{\frac{1}{3}}}{l(n-1)} \quad (1)$$

11
12
13 where s is the spacing between the electrode digits ($20 \mu\text{m}$), w is the width of the electrode (20
14
15 μm), l is the length (2 mm), and n is the number of digits (224). This process produced a cell
16
17 constant of $K_{\text{ide}} = 0.045 \text{ cm}^{-1}$. The measured conductance, G_{ecfet} , was converted to units of
18
19 conductivity by use of eq 2:

$$\sigma_{\text{ecfet}} = K_{\text{ide}} G_{\text{ecfet}} \quad (2)$$

30 31 **C. Physical Characterization of α -TiO₂**

32 *Electron Paramagnetic Resonance Spectroscopy*

33
34
35 Electron paramagnetic resonance (EPR) spectra were collected at 77 K using a Bruker
36
37 EMX X-band continuous-wave spectrometer. Data were collected for samples in liquid N_2 in a
38
39 finger Dewar. Samples were prepared by depositing 1500 ALD cycles of α -TiO₂ onto VWR
40
41 micro-cover glass slides ($0.15 \pm 0.02 \mu\text{m}$ thick). The slides were then diced into $2 \times 2 \text{ mm}^2$
42
43 pieces using a Dynatex GST-150 scribe-breaker. The diced samples were then placed in EPR
44
45 tubes.
46
47
48

49
50 Due to sample variations, all of the TiO₂ ($50 \text{ }^\circ\text{C}$, $100 \text{ }^\circ\text{C}$, $150 \text{ }^\circ\text{C}$ TiCl₄ and TDMAT) films
51
52 were of slightly different thickness as measured by ellispometry. To ensure a uniform amount of
53
54 TiO₂ was maintained between samples, the total area was varied. For instance, if the TDMAT
55
56
57
58
59
60

1
2
3 and 50 °C TiCl₄ TiO₂ had a thickness of 68 and 62 nm, respectively, then the area ratio of
4
5 TDMAT:50 °C TiCl₄ TiO₂ was adjusted to 1.0:1.1, to ensure an equivalent amount of TiO₂.
6

7 *Photoelectron Spectroscopy*

8
9
10 X-ray photoelectron spectroscopic (XPS) data were collected on ALD-deposited *a*-TiO₂ on
11
12 p⁺-Si using a Kratos Axis Ultra system with a base pressure of 1×10⁻⁹ Torr. The x-ray source
13
14 was a monochromatic Al Kα line at 1486.6 eV. Photoelectrons were collected at 0° from the
15
16 surface normal with a retarding pass energy of 160 eV for survey XPS scans, 10 eV for high-
17
18 resolution core levels, and 20 eV for valence-band XPS scans.
19

20
21 Work function measurements were performed using He I ultraviolet photoelectron
22
23 spectroscopy (UPS) on the Kratos Axis Ultra system. A pass energy of 5 eV was used in
24
25 conjunction with an aperture of 110 μm. Prior to the measurements, pure metal samples
26
27 (>99.99%) were sputter cleaned for 30 min with 4 kV Argon Ions. The work function (ϕ_{WF}) was
28
29 calculated from the measured spectra on a kinetic energy scale using eq (3):
30
31

$$32 \quad \phi_{WF} = E_{sec,meas} - E_{F,meas} + 21.21 \quad (3)$$

33
34 where $E_{sec,meas}$ and $E_{F,meas}$ are the measured energy of the secondary electron cutoff and the
35
36 Fermi energy, respectively, and 21.21 eV is the photon energy for He I excitation. The secondary
37
38 electron cutoff and Fermi energy were obtained by calculating the intercept of a linear fit of the
39
40 steep electron cutoff to that of the background and by fitting a Fermi distribution to the valence-
41
42 band maximum, respectively.
43
44
45

46 *Secondary-Ion Mass Spectroscopy*

47
48
49 Secondary-ion mass spectroscopy (SIMS) data were collected on a Cameca SIMS-7f GEO.
50
51 A 100 μm × 100 μm area of the sample surface was ionized and sputtered by a 7 keV Cs⁺
52
53 primary ion beam with no substrate biasing. A mass spectrometer collected and analyzed the
54
55
56
57
58
59
60

1
2
3 ejected secondary ions. The count rates of ^{30}Si , ^{48}Ti , $^{12}\text{C} + ^{133}\text{Cs}$ and $^{14}\text{N} + ^{133}\text{Cs}$ were collected
4
5 as a function of sputtering cycle. SIMS data were collected for all TDMAT and TiCl_4 *a*- TiO_2
6
7 films.
8
9

10 *Attenuated Total Reflection Infrared Spectroscopy*

11
12 Attenuated Total Reflection Infrared Spectroscopy (ATR-IR) spectra were collected using
13
14 a Thermo Scientific Nicolet 6700 optical spectrometer equipped with thermoelectrically cooled
15
16 deuterated L-alanine-doped triglycine sulfate (DLATGS) detector, electronically temperature-
17
18 controlled (ETC) EverGlo mid-IR source, $\text{N}_2(\text{g})$ purge, KBr beam splitter, and diamond ATR
19
20 crystal single-reflection Smart-iTR accessory. After data collection, spectra for ALD films on
21
22 glass substrate were corrected using pristine glass as the background. Air was used as
23
24 background for ALD films deposited on silicon substrate. In addition, the baseline was flattened
25
26 when needed. TIRS data collection and processing was performed using OMNIC software
27
28
29
30
31 v.9.2.41.
32

33 **D. Electrochemical Characterization**

34
35 Electrochemical data were obtained using a BioLogic SP-200 potentiostat in a three-
36
37 electrode configuration with 1.0 M $\text{H}_2\text{SO}_4(\text{aq})$ as the electrolyte. A carbon rod (Strem
38
39 Chemicals, 99.999%) was used as the counter electrode, and a Hg/HgSO_4 electrode (Gamry
40
41 Instruments) was used as the reference electrode. An ELH-type tungsten-halogen lamp provided
42
43 light that passed through a quartz diffuser to reach the Pyrex electrochemical cell. The
44
45 illumination intensity was measured by a Si photodiode (Thorlabs) and the light intensity was
46
47 adjusted to produce the same current on the photodiode as was produced by illumination with
48
49 100 mW cm^{-2} of Air Mass 1.5 sunlight. Cyclic voltammetric data were collected at a 40 mV s^{-1}
50
51
52
53
54 scan rate.
55
56
57
58
59
60

III. Results

A. Work Functions of the Metals

Figure S1 shows representative work function measurements by UPS for Ni, Pd, Pt, Ir and Au. The spectra allowed determination of the work functions for these polycrystalline metals (purity >99.99 %) as: 5.09 ± 0.4 , 5.27 ± 0.2 , 5.56 ± 0.07 , 5.32 ± 0.2 , and 5.05 ± 0.3 eV for Ni, Pd, Pt, Ir, and Au, respectively. These work function values are in good agreement prior work function measurements on polycrystalline metals.³⁶⁻³⁸ The work functions of Mg and Ti were taken to be 3.66 ± 0.2 , and 4.33 ± 0.2 eV, respectively.³⁶

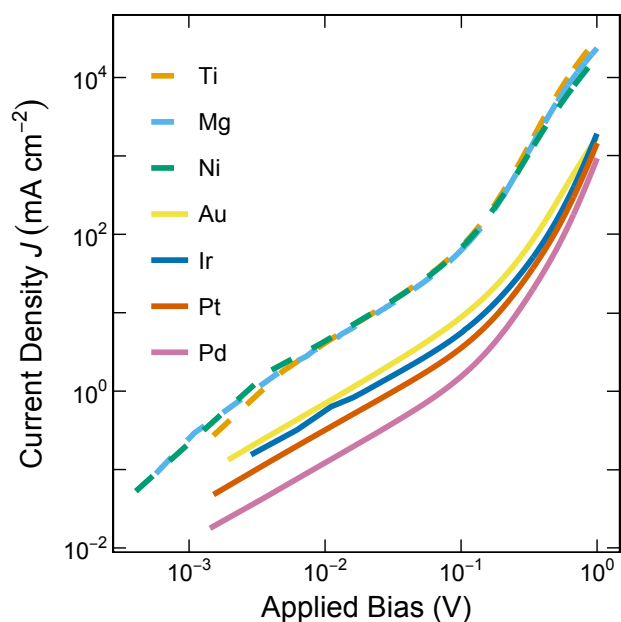
B. Conductivity of p^+ -Si/ a -TiO₂/metal Devices

J-V Characteristics of p^+ -Si/ a -TiO₂/metal Devices

Figure 1 shows representative solid-state $J-V$ characteristics for p^+ -Si/ a -TiO₂/metal devices with a -TiO₂ grown on the p^+ -Si substrates via 1500 ALD cycles using a TDMAT precursor and substrate temperature of 150 °C. The ALD procedure yielded ~ 68 nm thick a -TiO₂ films. The $J-V$ characteristics showed ohmic (linear) behavior at biases < 50 mV. **Figure S2** shows the normalized differential conductance as a function of applied bias for a p^+ -Si/ a -TiO₂/Ni device, which is consistent with behavior typical of dielectric films.^{39 40}

The current density passed as a function of applied bias depended on the top contact, **Figure 1**, with devices having Ti, Mg or Ni top contacts behaving almost mutually identically, especially at low biases. At the same applied bias, devices with Au, Ir, Pt or Pd top contacts passed $\leq 10\%$ of the current densities of devices having Ti, Mg or Ni as a top contact. For example, at an applied bias of 0.1 V, devices with Ti, Mg, or Ni top contacts passed current densities of ~ 60 mA cm⁻², as compared to the current densities passed by devices with Au (8.7 mA cm⁻²), Ir (5.5 mA cm⁻²), Pt (3.6 mA cm⁻²), or Pd (1.5 mA cm⁻²) contacts. Compared to

1
2
3 devices with Ti, Mg or Ni top contacts, the devices with Au, Ir, Pt or Pd top contacts required an
4
5 additional 90 – 250 mV of bias to pass current densities of 10 mA cm^{-2} , as well as an additional
6
7 150 – 330 mV of bias to pass current densities of 30 mA cm^{-2} . The conductivities at low applied
8
9 biases ($< 50 \text{ mV}$) were determined from linear fits of the data (**Figure 1**). The contact
10
11 resistances were determined by transmission line measurements, and the compensated voltages
12
13 between different metal contacts were measured for all devices (**Table S1**). Although the
14
15 contact resistance increased as the work function of the metal increased, the metals with the
16
17 higher work functions yielded sufficiently low current densities that the total voltage
18
19 compensation would not create a noticeable change in the J - V behavior over the measurement
20
21 range depicted in **Figure 1**.
22
23
24
25



26
27
28
29
30
31
32
33
34
35
36
37
38
39
40
41
42
43
44
45
46 **Figure 1.** Current density (J) vs applied bias (V) for solid-state p^+ -Si/ a -TiO₂/metal devices. The
47
48 a -TiO₂ was $\sim 68 \text{ nm}$ thick. The devices were tested in a two-electrode configuration, and the
49
50 bias was applied across the device using the p^+ -Si side as the working electrode and the metal
51
52 side as the counter electrode.
53
54
55
56
57
58
59
60

Table 1. Conductivities for the devices with varied metal contacts as determined from a fit of the J - V behavior in the low-bias regions. At least 5 samples with each metal were tested, and error estimates represent one standard deviation.

Top Contact	Conductivity (S cm^{-1})	Work Function (eV)
Ti	$(85 \pm 18) \times 10^{-5}$	4.33 ± 0.20
Mg	$(85 \pm 1.2) \times 10^{-5}$	3.66 ± 0.20
Ni	$(95 \pm 4.0) \times 10^{-5}$	5.09 ± 0.39
Au	$(13 \pm 1.7) \times 10^{-5}$	5.05 ± 0.30
Ir	$(4.0 \pm 1.6) \times 10^{-5}$	5.32 ± 0.18
Pt	$(8.3 \pm 1.8) \times 10^{-5}$	5.56 ± 0.07
Pd	$(2.3 \pm 0.45) \times 10^{-5}$	5.27 ± 0.18

Space-Charge-Limited Current (SCLC) Spectroscopy

Figure 2a shows a plot of the J - V characteristics for a $\text{p}^+\text{-Si}|a\text{-TiO}_2|\text{Pt}$ device, extended to 5 V of applied bias. At ~ 5 V, the current increased abruptly, consistent with a space-charge limited current in the trap-free regime.⁴¹⁻⁴⁴ **Figures S3a-c** show similarly extended J - V characteristics for devices with Au, Ir or Pd contacts. The number of traps, the majority charge-carrier mobility, and the charge-carrier concentration were calculated from the threshold voltages for trap filling, the J - V behavior in the trap-free regime, and the J - V behavior in the ohmic regime, respectively, according to eqs 4–6.⁴¹⁻⁴⁴

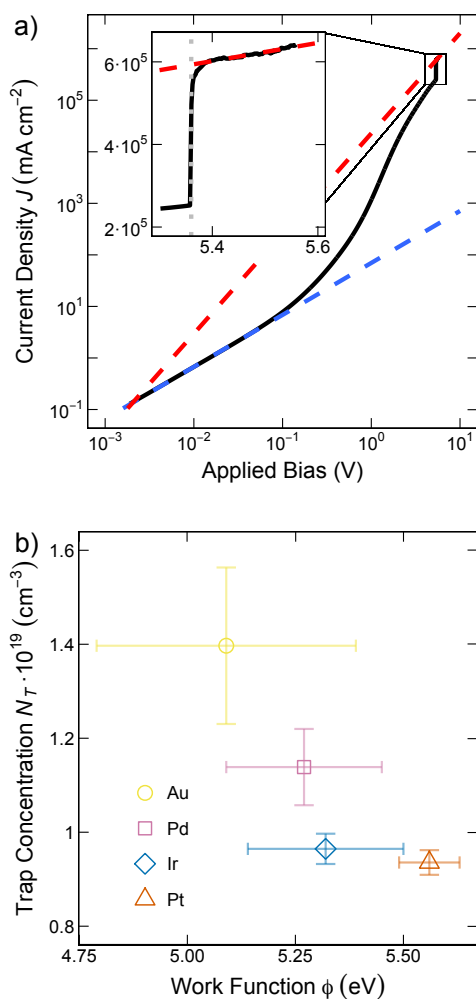
$$V_{TF} = \frac{qN_T L^2}{\epsilon_0 \epsilon} \quad (4)$$

$$J_{TF} = \frac{9\epsilon\mu V^2}{8L^3} \quad (5)$$

$$J_{\Omega} = \frac{qn\mu V}{L} \quad (6)$$

where V_{TF} is the threshold voltage for trap filling, J_{TF} is the current density in the trap-free region, J_{Ω} is the current density in the ohmic region, q is the absolute charge of an electron, N_T is the trap density, L is the thickness of the sample, ϵ_0 is the permittivity of free space, ϵ ($= 112$) is the dielectric constant of TiO_2 , μ is the mobility of the majority carriers, and n is the mobile charge-carrier density. The calculated trap densities, mobilities, and effective mobile charge-carrier densities for $\text{p}^+\text{-Si}|a\text{-TiO}_2|\text{metal}$ devices with various metal top contacts are tabulated in

Table S2.



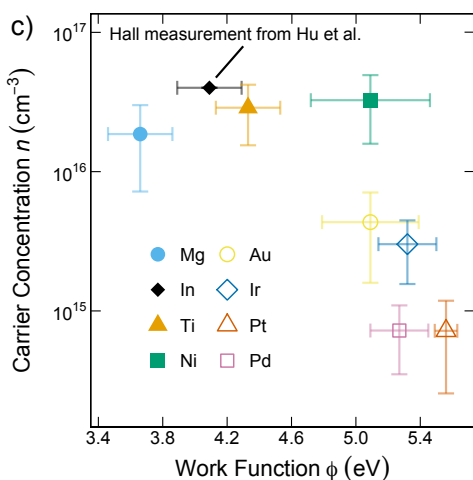


Figure 2. a) J - V characteristics of a solid-state $\text{p}^+\text{-Si}|a\text{-TiO}_2|\text{Pt}$ device, extended to applied biases > 5 V. The $a\text{-TiO}_2$ was ~ 68 nm thick. The inset is a plot of the crossover into the trap-filled regime. Linear regressions are shown for the ohmic region at low bias (blue dashed line), and the trap-filled space-charge-limited regimes (red dashed line in the inset). b) Concentration of trap states for devices with top contacts to high-work-function metals. c) Calculated free-carrier concentrations for varied metal top contacts.

Figure 2b shows the dependence of the number of traps measured by SCLC spectroscopy on the work function of the top contact used for the $\text{p}^+\text{-Si}|a\text{-TiO}_2|\text{metal}$ device.^{36, 45-46} The number of traps measured by SCLC decreased only slightly as the work function of the top contact increased. For low-work-function metals, the trap concentration could not be measured before the voltage limits of the potentiostat were reached, implying trap densities $> 1.5 \times 10^{19} \text{ cm}^{-3}$.

Figure 2c shows the variation of the calculated free-carrier concentration for each metal contact as a function of the work function of each metal. The free-carrier concentration was calculated by using the value of the mobility found in the trap-free regime (eq 5) with a Pt contact ($6.5 \pm 3 \times 10^{-4} \text{ cm}^2 \text{ V}^{-1} \text{ s}^{-1}$), in conjunction with the slopes of the ohmic regions for the various top contacts, according to eq 6. Below a work function of ~ 5.2 eV, the (averaged) carrier concentration was essentially independent of the work function of the top metal contact,

whereas for a work function > 5.2 eV, the (averaged) free-carrier concentration becomes dependent on the work function and thus decreased by $10^1 - 10^2$ cm^{-3} . Although the mobility is not a constant for different dopant concentrations, the mobility was approximated to be independent of the free-carrier concentrations. This approximation is in agreement with the free-carrier density measured previously by Hall measurements with In contacts (**Figure 2c**).⁴ In addition, the mobility measured is in agreement with the predicted mobility of 2×10^{-4} $\text{cm}^2 \text{V}^{-1} \text{s}^{-1}$ by Pham et al using DFT+U methods.⁴⁷

AC Conductivity

Figure 3 shows the AC conductivity as a function of frequency for a $\text{p}^+\text{-Si}|a\text{-TiO}_2|\text{Ni}$ device at room temperature and under an applied bias of 300 mV. The conductivity of the sample was 3.0×10^{-6} S cm^{-1} for frequencies $\leq 10^5$ Hz, and increased exponentially at frequencies $> 1 \times 10^4$ Hz.

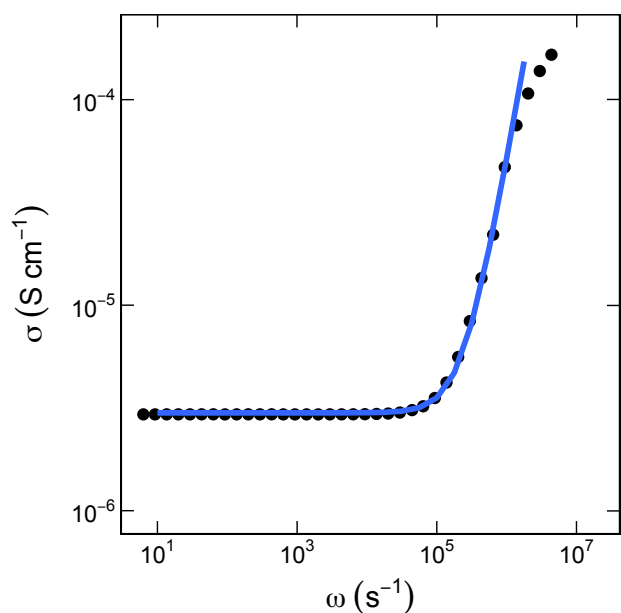


Figure 3. AC conductivity of a solid-state $\text{p}^+\text{-Si}|a\text{-TiO}_2|\text{Ni}$ device measured in a two-electrode configuration with a bias of 300 mV applied between the $\text{p}^+\text{-Si}$ side and the Ni side of the device. The blue line shows a fit of the frequency-dependent region of the data to a power-law model,

$\sigma(\omega) = \sigma_{DC} + A\omega^s$, where $\sigma_{DC} = 9.9 \times 10^{-17} \text{ S m}^{-1}$, $A = 2.96 \times 10^{-6} \text{ S m}^{-1}$, and $s = 1.95$.

Temperature-Dependent Conductivity of Ni| a -TiO₂|Ni Devices

Figure 4 shows the conductivity as a function of temperature for a Ni| a -TiO₂|Ni through-layer device in which the thickness of the a -TiO₂ layer was 68 nm, measured at temperatures between 10 K and 310 K. The data showed two regions, each with an Arrhenius-type exponential temperature dependence. Activation energies for charge transport were calculated from the slopes of the linear fits. The model yielded an activation energy for charge transport at temperatures in the 250 – 310 K range of $350 \pm 15 \text{ meV}$, which is substantially larger than the $\sim 7 \text{ meV}$ activation energy calculated for charge transport at temperatures in the 100 – 125 K range. The activation energy continuously decreased as the temperature decreased.

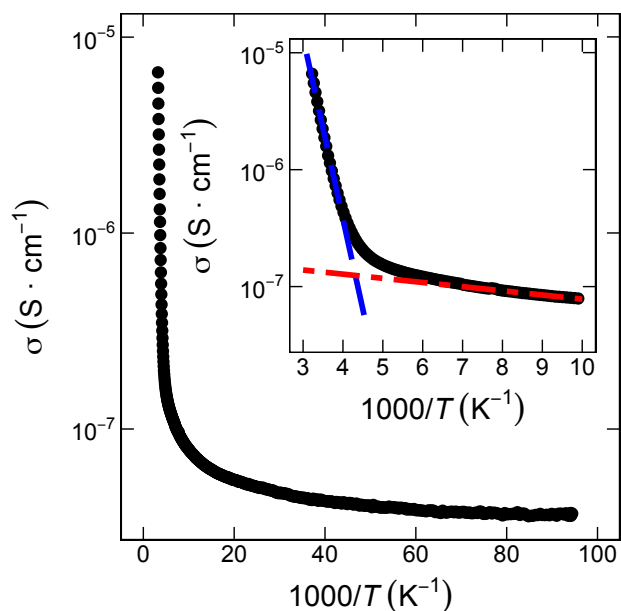


Figure 4. Temperature-dependent conductivity of a Ni| a -TiO₂|Ni device in which the thickness of the a -TiO₂ layer was 68 nm. The inset shows the same data for the 100 – 310 K temperature range; the blue and red dashed lines are linear fits of the data for temperatures in the range of 250 – 310 K, and 100 – 125 K ranges, respectively.

Potential-Dependent Conductivity of a -TiO₂

1
2
3 **Figure 5** shows the dependence of the conductivity on the gate potential (V_{gate}) for an *a*-
4 TiO₂ film with Ti contacts in the EC-FET configuration in contact with 1.0 M H₂SO₄(aq), which
5 allowed the conductivity of the TiO₂ to be measured as a function of the potential, or Fermi
6 level, of the gate electrode. V_{gate} was referenced against a reversible hydrogen electrode (RHE)
7 and was varied across a potential range relevant to water splitting (-0.4 to +1.75 V versus RHE).
8 The data showed a sharp increase in conductivity as V_{gate} became more negative than -0.3 V
9 versus RHE, indicating a sharp increase in electron transport in the conduction band. At these
10 potentials the TiO₂ is in accumulation. At more positive potentials, the conductivity showed a
11 weak dependence on V_{gate} , and decreased by ~ 1% over a range of 2 V. These data suggest the
12 presence of a finite density of states at potentials extending for >2 eV below the TiO₂
13 conduction-band edge. These results generally agree with data for Si|*a*-TiO₂ and Si|*a*-TiO₂|Ni
14 samples observed under electrochemical conditions in 1.0 M KOH(aq). The Si|*a*-TiO₂ showed a
15 flat-band potential of -0.9 vs Ag/AgCl, i.e. +0.1 V versus RHE, whereas the Si|*a*-TiO₂|Ni sample
16 showed Fermi-level pinning over a broad potential range (0 to 1.4 V versus RHE).^{17, 48}

17
18
19
20
21
22
23
24
25
26
27
28
29
30
31
32
33
34
35
36
37
38
39
40
41
42
43
44
45
46
47
48
49
50
51
52
53
54
55
56
57
58
59
60
The conductivity measured for *a*-TiO₂ using the IDE in 1.0 M H₂SO₄(aq) was $1.17 \pm 0.45 \times$
 $10^{-5} \text{ S cm}^{-1}$, with three samples measured (**Table S3**). Measurements made in air using one of the
IDEs used in the EC-FET experiments showed a dry conductivity equal to that for the electrode
in contact with the electrolyte, suggesting that the IDE electrode was unaffected by immersion in
the electrolyte, and indicating negligible electrolyte-induced effects on the conductivity.

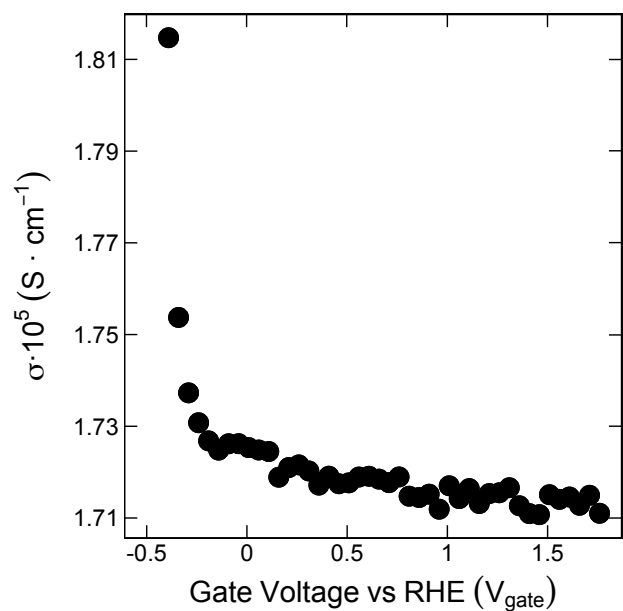


Figure 5. Conductivity of *a*-TiO₂ as a function of the gate voltage (V_{gate}) applied to interdigitated contacts covered by 1500 cycles (approximately 68 nm) of *a*-TiO₂.

C. Effects of ALD Process on Physical Characteristics of ALD *a*-TiO₂

J-V Characteristics of p^+ -Si|*a*-TiO₂|Ni Devices

Figure 6 shows the *J-V* characteristics of p^+ -Si|*a*-TiO₂|Ni devices, with the *a*-TiO₂ films prepared via ALD using either a TDMAT precursor with the substrate held at 150 °C or a TiCl₄ precursor with the substrate held at 50, 100 or 150 °C. Films deposited from TDMAT at 150 °C or from TiCl₄ at 50 or 100 °C had undetectable levels of crystallinity, whereas small fractions of crystallinity were detected from films prepared at 150 °C, as measured by Raman spectroscopy and glancing incidence X-ray diffraction (**Figures S4a,b**).⁴⁹⁻⁵⁰ In addition, the main phase of the films were probed by FTIR. No evidence was found to support the presence of H₂TiO₃ in the films deposited on glass and Si (**Figures S5a,b**).

All of the TiO₂ devices exhibited ohmic regions at low biases, however for the same applied bias, the TDMAT-TiO₂ film passed a more than an order of magnitude higher current

density than the least resistive $\text{TiCl}_4\text{-TiO}_2$ film. The conductivities of the $\text{TiCl}_4\text{-TiO}_2$ films increased with growth temperature. The mobilities of the various TiO_2 films were calculated according to eq 5, and the free-carrier concentrations were calculated using eq 6. The free-carrier concentrations for the $\text{TiCl}_4\text{-TiO}_2$ films were smaller by one to three orders of magnitude than that of the TDMAT film.

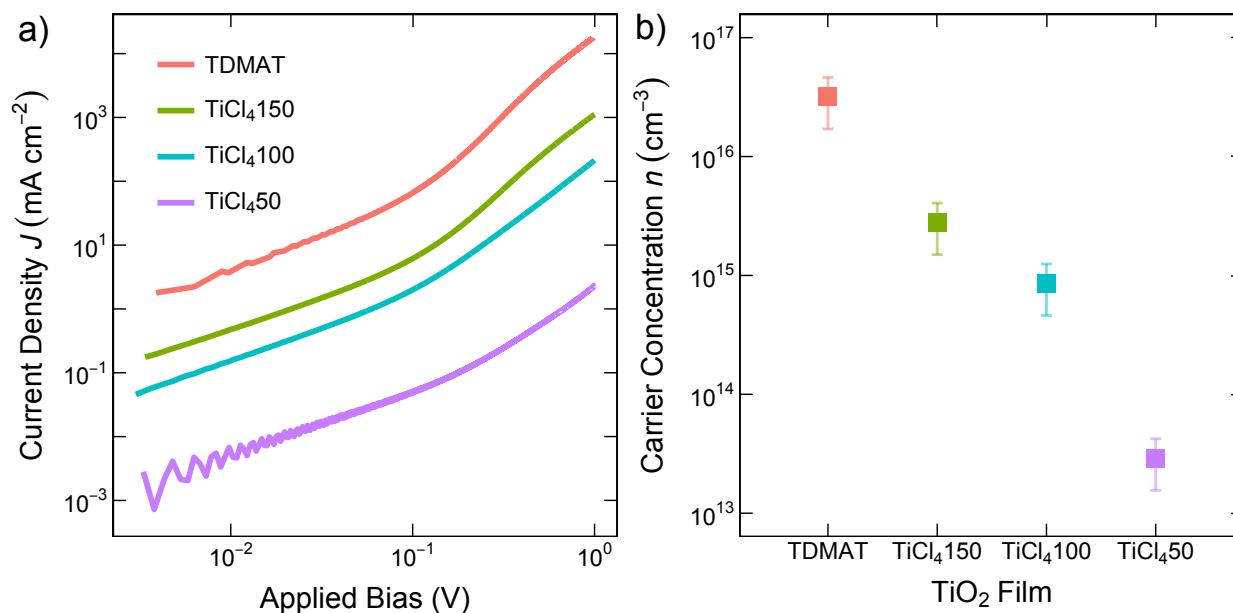


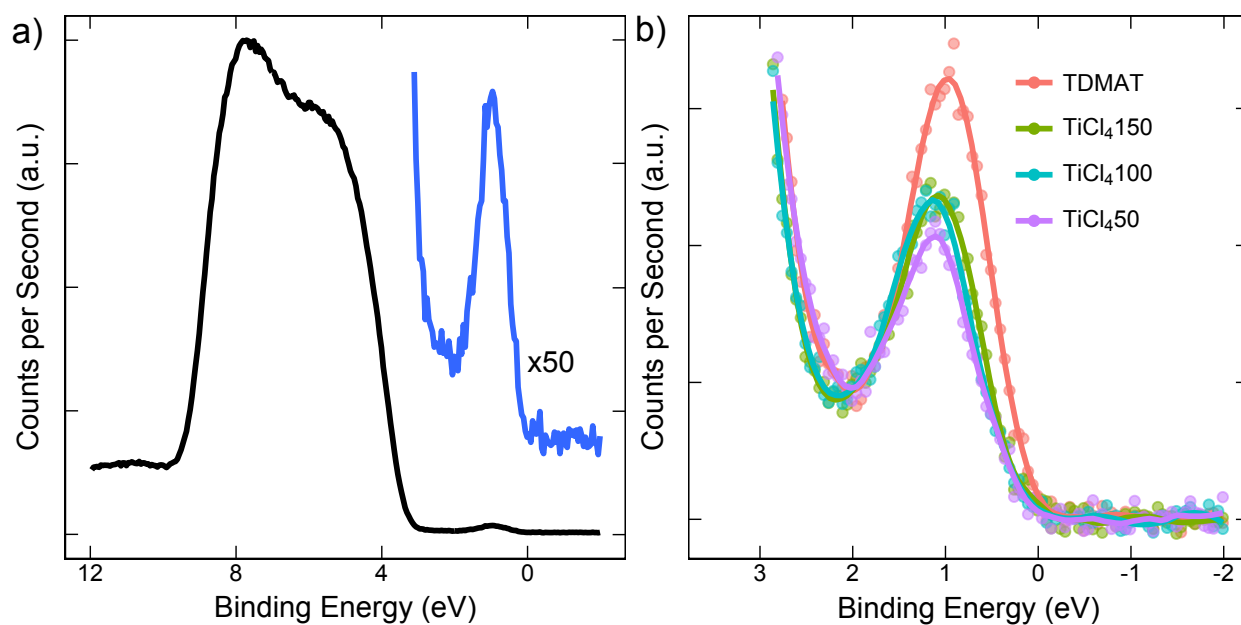
Figure 6. a) J - V characteristics and b) free-carrier concentrations calculated for various TiO_2 films grown on $\text{p}^+\text{-Si}$ substrates and contacted with Ni. The film grown from TDMAT at 150 °C was ~ 68 nm thick; the films grown from TiCl_4 were ~ 60 nm thick and were grown at varied temperatures of 50, 100, or 150 °C.

Valence-Band Spectra

Figure 7a shows the XPS valence-band spectra for an $\alpha\text{-TiO}_2$ film prepared by ALD using a TDMAT precursor at 150 °C. The observed signal was in accord with previously reported valence-band spectra of identically prepared $\alpha\text{-TiO}_2$.^{4, 18} After a Shirley background was subtracted, the spectra showed a peak centered at 1.07 ± 0.07 eV with a full width a half maximum, FWHM, of 0.83 eV. Using the previously determined position of the Fermi level in

1
2
3 TiO₂ as 0.40 eV below the CBM, the defect band was centered at 1.47 eV and extended from ~ 1
4 – 1.9 V below the CBM, i.e. from ~ 0.6 – 1.5 eV below the Fermi level.¹⁶ Previous analysis has
5
6
7 located the center of the defect band at ~ 1.34 eV below the CBM, with a FWHM of 0.83 eV,
8
9
10 consistent with the results described herein.¹⁶

11
12 **Figure 7b** presents the valence-band spectra of ALD-TiO₂ films prepared using different
13 precursors and growth temperatures. All of the valence-band spectra showed a peak at $1.07 \pm$
14 0.07 eV, with mutually similar FWHMs. The TDMAT-TiO₂ film exhibited the largest valence-
15 band signal, while the TiCl₄-TiO₂ films exhibited weaker signals that increased with growth
16
17 band signal, while the TiCl₄-TiO₂ films exhibited weaker signals that increased with growth
18
19 temperature. The relative peak intensities (normalized to the largest signal) were 0.62 ± 0.2 , 0.69
20 ± 0.2 , 0.71 ± 0.3 and 1 ± 0.6 , for the TiCl₄-TiO₂ films grown at 50 °C, 100 °C, 150 °C, and
21
22 TDMAT-TiO₂, respectively.
23
24
25
26
27



51
52 **Figure 7.** a) X-ray photoemission spectra (without background subtraction) for the valence band
53 of *a*-TiO₂ grown via ALD using a TDMAT precursor at 150 °C. b) Comparison of the X-ray
54 photoemission valence-band spectra of ALD *a*-TiO₂ films grown using a TDMAT precursor at
55 150 °C, or a TiCl₄ precursor at 50 °C, 100 °C or 150 °C.
56
57
58
59
60

Electron Paramagnetic Resonance Spectroscopy

Figure 8 compares the EPR spectra for the various ALD-TiO₂ films. The isotropic g-values extracted from the spectra were 1.939 and 2.000. The broad signal at 1.939 is consistent with the presence of Ti³⁺ since the signal is within the range of previously reported g-values, g = 1.92 to 2.00, for Ti³⁺ sites.⁵¹⁻⁵⁶ The TDMAT-TiO₂ films exhibited a substantially larger Ti³⁺ signal than the TiCl₄-TiO₂ films. The TiCl₄-TiO₂ films grown at 150 °C and 100 °C exhibited a detectible signal for Ti³⁺, while the TiCl₄-TiO₂ grown at 50°C showed no appreciable Ti³⁺ signal.

The signal at 2.000 observed in the spectra for 150 °C TiCl₄-TiO₂ film is attributable to either the variations of impurities within the glass substrate or electrons trapped at oxygen vacancy sites.^{26, 57} The sharpness of the signal as well as appearance at g-values greater than the broad Ti³⁺ signal is consistent with the electrons trapped at oxygen vacancy sites. Additional control experiments showed that only a decrease in the signal at this g-value was observed with the substrate-only and EPR silent Al₂O₃ signal, as can be seen in **Figure S7a**. The same decrease was present in all other TiO₂ films but was not observed in the background (cavity-only) signal, which had no prominent features.

In addition, EPR measurements were performed at various angles of rotation. No shift was observed when the TDMAT *a*-TiO₂ sample was rotated within the EPR instrument. This result is expected as *a*-TiO₂ samples have an amorphous structure and the samples are macroscopically arranged randomly in the EPR tube. The results of the control experiments are presented in **Figure S7b**.

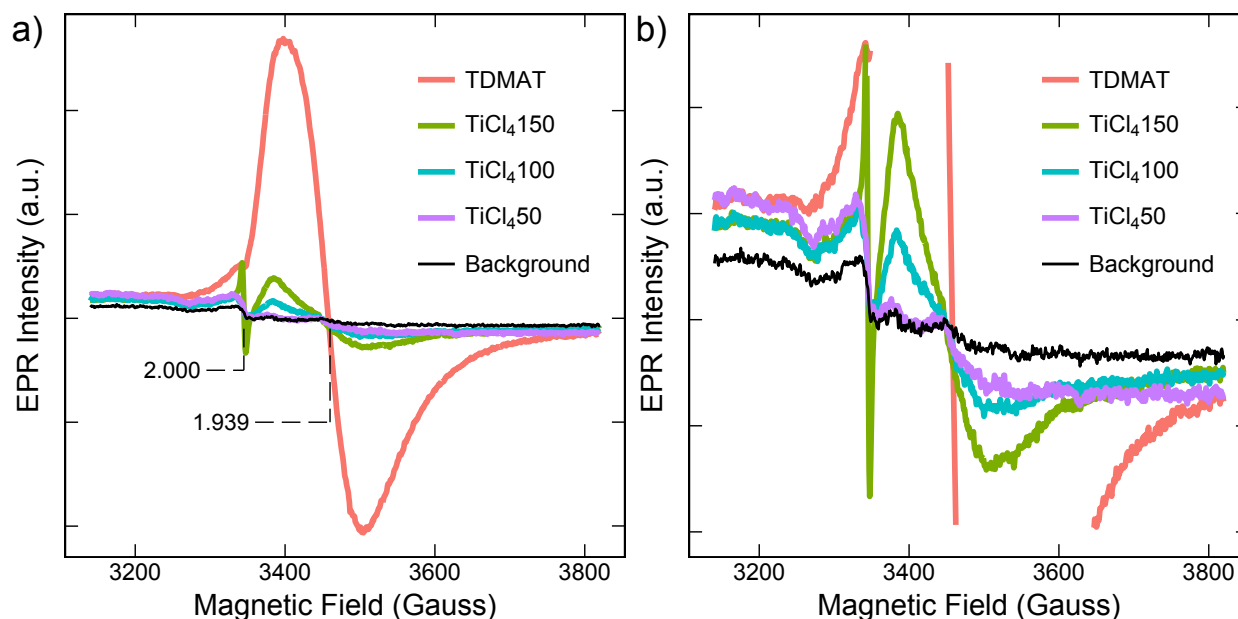


Figure 8. a) Electron paramagnetic resonance (EPR) spectroscopy for *a*-TiO₂ films grown via ALD using a TDMAT precursor at 150 °C, or a TiCl₄ precursor at 50 °C, 100 °C or 150 °C. b) EPR spectra rescaled to show the detail of the smaller peaks. The background spectrum includes the EPR tube and the glass substrate.

D. Application to Photoelectrochemical Water Oxidation in Acidic Aqueous Electrolytes

Figure 9 shows the voltammetric behavior of non-photoactive p⁺-Si|*a*-TiO₂|Ir anodes and n-Si|*a*-TiO₂|Ir photoanodes under 1 Sun illumination in 1.0 M H₂SO₄(aq). The Ir was deposited on the *a*-TiO₂ as catalytic islands 3 μm in diameter on a 7 μm pitch. The Ir islands were 35 nm thick, and were deposited either directly on the *a*-TiO₂ or onto 35 nm of Ti on the *a*-TiO₂. Ti was selected as an intermediate contact because p⁺-Si|*a*-TiO₂ devices with Ti contacts had exhibited high conduction relative to devices with Ir contacts. The samples with the Ti interconnect performed substantially better than those without the Ti interconnect, as evidenced by a reduction in the overpotential required to reach 10 mA cm⁻² of current density of 280 mV for the Ti|Ir n-Si devices and of 460 mV for the Ti|Ir p⁺-Si devices.

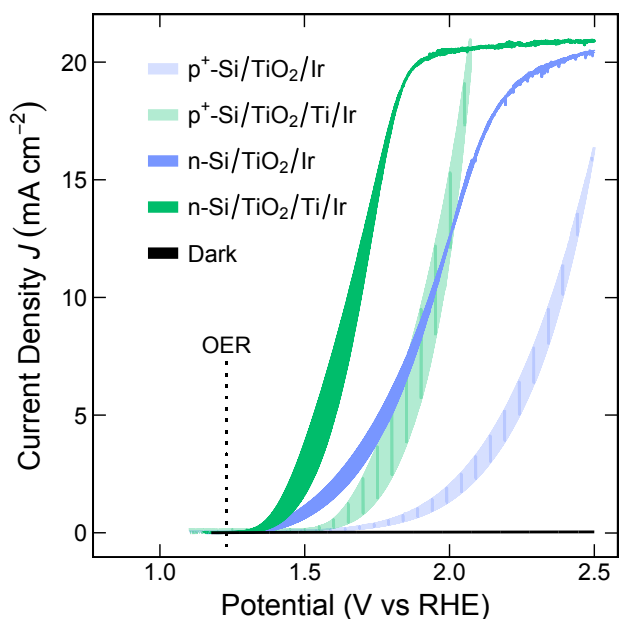


Figure 9. Cyclic voltammetry of non-photoactive p^+ -Si/ a -TiO₂ anodes and n-Si/ a -TiO₂ photoanodes in contact with 1.0 M H₂SO₄. The samples were p^+ -Si and n-Si substrates coated with 1500 ALD cycles of a -TiO₂ onto which metal-island top contacts were deposited. The metal top contacts to the a -TiO₂ layer were 35 nm thick islands of Ir, 3 μ m in diameter pitched 7 μ m apart, deposited either directly on the a -TiO₂ or onto a 35 nm thick Ti island interconnect. The CV sweep was conducted in the dark and 1 sun illumination for p^+ -Si and n-Si, respectively, from 1.1 V vs RHE to 2.5 V vs RHE at scan rate of 40 mV s⁻¹.

IV. Discussion

A. Identity and Position of Defect States in ALD a -TiO₂

The valence-band spectra for a -TiO₂ deposited via ALD showed a small peak within the band gap of the TiO₂, centered at 0.94 eV below the Fermi level.^{18,39} The band had a FWHM of 0.83 eV, indicating that a wide energy band exists within the band gap. Defect bands in TiO₂ have been observed both for amorphous films grown by ALD as well as crystalline films grown by various methods.⁵⁸⁻⁶⁴ The bands have been associated with oxygen and/or other defects on the surface of the TiO₂. Oxygen vacancy sites are often implicated and have been observed by TEM.⁵⁹ The defect band has been correlated with the introduction of imperfections into the crystal.^{47,65} Oxygen vacancies would provide doping and produce Ti³⁺ sites by the trapping of free electrons into localized Ti-O octahedra with an oxygen vacancy.⁶⁶ Theoretical calculations

1
2
3 favor oxygen vacancies as the structural origin of the defect sites, and calculations moreover
4
5 have been used to calculate conduction by small polaron hopping.^{47, 67-70}
6

7
8 Oxygen defects and Ti^{3+} sites dominate the physical and chemical properties in TiO_2 .^{64, 66,}
9
10 ^{68, 71-76} The bulk structure of reduced crystalline TiO_{2-x} contains defects of doubly charged
11
12 oxygen vacancies, interstitial titanium defects, and other defects.⁷⁷ The defects vary with the
13
14 amount of the oxygen deficiency²³ and vacancies on the surface have been imaged by scanning
15
16 tunneling microscopy.⁷⁷⁻⁷⁸ The number of vacancies can be controlled by the method of
17
18 annealing, and surface vacancies can be healed by dosing with oxygen.²³ Additionally, self-
19
20 doping of TiO_2 from oxygen vacancies yields Ti^{3+} sites.²⁸
21
22

23
24 ALD TiO_2 grown at substrate temperatures < 300 °C has been shown to be amorphous
25
26 when annealed below 350 °C but becomes crystalline when annealed above 350 °C.⁷⁹⁻⁸⁰ XPS
27
28 studies of ALD *a*- TiO_2 have observed both a Ti^{3+} shoulder on the Ti 2p core level, and a small
29
30 shoulder on the O1s spectra that is assigned to -OH groups on the surface.⁶²⁻⁶³ Both normal and
31
32 resonant valence band spectra show a peak at ~ 1 eV below the Fermi level that is due to
33
34 titanium and attributable to Ti^{3+} states. The band is much weaker in crystalline TiO_2 .⁶³
35
36

37
38 XPS depth profiling was forgone because the Ti 2p XPS spectrum is heavily altered after
39
40 Ar ion bombardment. Oxygen is preferentially removed thus reducing the TiO_2 . The reduced
41
42 states observed in the spectrum generated from the Ar ion bombardment are thus not an accurate
43
44 representation of the underlying composition of the TiO_2 .⁸¹ Instead we focused on angle
45
46 dependent XPS spectroscopy where with increased electron emission angle Θ to the surface
47
48 normal the inelastic mean free path for electrons is reduced. The values for Al $K\alpha$ radiation are
49
50 given in **Table S4**.
51
52
53
54
55
56
57
58
59
60

1
2
3 The concentration of the defect states (and Ti^{3+} states) has been investigated by angle
4 dependent XPS.¹⁷ No change in Ti 2p core level and defect band were detected. However, with
5 increasing surface sensitivity a shoulder at 532.5 eV at the O 1s core level (attributed to
6 dumbbell di-oxygen species, OH-groups and/or to reconstruction of the TiO_2) was visible which
7 increased in intensity with increased Θ . Here, we performed scans for $\Theta=0$ and 70 with
8 improved signal to noise ratio which are shown in **Figure S8**. Again, no difference between bulk
9 or surface sensitive spectra could be observed indicating no surface re-oxidation of the defect
10 band.
11
12
13
14
15
16
17
18
19
20

21 EPR spectra provided direct evidence of Ti^{3+} within the bulk *a*- TiO_2 films (**Figure 8**).
22 The correlation between the strength of the Ti^{3+} signals in the EPR spectra and the strength of the
23 defect-band peaks in the XPS valence-band spectra supports the assignment of the defect peak in
24 the XPS valence-band spectra to localized Ti^{3+} sites. The films are amorphous, so the Ti^{3+} sites
25 can be expected to show a dispersion in energy due to differences in Ti–Ti and Ti–O bond
26 lengths,⁸² consistent with the wide peak (FWHM = 0.83 eV) observed for the defect band.
27
28
29
30
31
32
33
34

35 The Ti^{3+} sites in the ALD *a*- TiO_2 films were however not directly detectable by XPS.^{4, 18}
36 Hence, either the concentration of Ti^{3+} sites near the surface is below the detection limit of XPS,
37 or such sites may not be present on the surface of air-exposed samples due to oxidation of Ti^{3+} in
38 the presence of water and air.^{4, 53-54} The oxidation of surface Ti^{3+} sites would likely create a
39 surface layer that is more resistive than the bulk of the film, consistent with the low conductance
40 values measured when non-penetrative, soft contacts (e.g. Hg droplet or liquid electrolyte
41 contacts) were made to the ALD- TiO_2 films. Deposition of metal contacts by electron-beam
42 evaporation or sputtering would thus allow low-resistance contacts to be made to the ALD-
43
44
45
46
47
48
49
50
51
52
53
54
55
56
57
58
59
60

1
2
3 TiO₂,^{4, 16} consistent with expectations for penetration of a native resistive surface layer on these
4
5
6 *a*-TiO₂ films.

7
8 The *J-V* behavior for p⁺-Si|TiO₂|Ni devices formed with TiO₂ from varied ALD processes
9
10 shows that conduction through films of ALD *a*-TiO₂ is not limited to films produced from
11
12 TDMAT, although the conductivity of *a*-TiO₂ formed using TDMAT is greater than for films
13
14 formed using TiCl₄. Increases in the conductivities of the films correlated with increases in the
15
16 strengths of the EPR signals for Ti³⁺ as well as with increases in the amplitude of the defect peak
17
18 in the valence-band spectra. In combination, these data suggest that Ti³⁺ sites are important
19
20 contributors to the conductivities of the films.
21
22

23
24 Previously, the high conductivities of TDMAT-TiO₂ films were hypothesized to directly
25
26 arise from an increased density of C and N impurities.^{4, 18} The C and N impurities were measured
27
28 for all films (TDMAT, 150 °C, 100 °C and 50 °C TiCl₄ films) via SIMS, which revealed very
29
30 similar concentrations of C and N impurities in all of the samples despite the large range in
31
32 observed film conductivity. The C and N impurities thus appear to be independent of the
33
34 precursor and preparation of the *a*-TiO₂ film, unlike the concentration of Ti³⁺ sites. The
35
36 normalized SIMS spectra for C and N are displayed in **Figure S10**.
37
38

39 40 **B. Conduction through the *a*-TiO₂ Bulk**

41 42 *Temperature-Dependent Conductivity*

43
44
45 The temperature-dependent conductivity for temperatures > 250 K of Ni|*a*-TiO₂|Ni
46
47 layered stacks showed Arrhenius-type behavior, with an activation energy of 350 meV and a
48
49 prefactor of ~ 0.4. The observed activation energy suggests a Marcus type of reorganization
50
51 energy of 1.4 eV.⁸³ A transition was observed from Arrhenius-type behavior in the high-
52
53 temperature limit (> 250 K) to temperature-independent tunneling type behavior at low
54
55
56
57
58
59
60

1
2
3 temperatures (< 50 K). Similar behavior has been observed with NiO.⁸⁴ In addition, analogous
4
5 behavior has also been observed for sputtered TiO₂ films, even though the sputtered TiO₂ films
6
7 had 3–4 orders of magnitude higher conductivities than the α -TiO₂ films produced herein.⁸⁵⁻⁸⁶
8
9 For crystalline rutile and anatase TiO₂, small-polaron or variable-range hopping between Ti³⁺
10
11 sites and adjacent Ti⁴⁺ sites is most commonly thought to be the primary conduction mechanism,
12
13 and theory has been used to model small-polaron hopping in both crystalline and amorphous
14
15 TiO₂.^{47, 58, 70, 87-89} Pham et al. have used DFT+U methods to calculate a reorganization energy for
16
17 charge transfer between Ti³⁺ and Ti⁴⁺ sites in α -TiO₂ of 1.14 eV, while Deskins and Dupuis have
18
19 used similar methods to estimate an activation energy for polaron hopping in both rutile and
20
21 anatase TiO₂ of ~ 0.3 eV.^{47, 75} Both estimates are consistent with the results reported herein.⁴⁷
22
23 Assuming that the density of Ti³⁺ sites is equal to the measured trap-site density ($\sim 10^{19}$ cm⁻³)
24
25 yields an average distance between Ti³⁺ sites of ~ 4 nm, whereas Ti–Ti distances in TiO₂ rutile or
26
27 anatase crystals are 0.30 – 0.46 nm.⁹⁰⁻⁹¹
28
29
30
31

32 *Frequency-Dependent Conductivity*

33
34
35 The AC conductivity of Ni| α -TiO₂|p⁺-Si devices was constant (3.0×10^{-6} S cm⁻¹) for
36
37 frequencies $\leq 10^5$ Hz, and increased rapidly for frequencies above 10^6 Hz. For charge transport
38
39 within the conduction band or valence band of a semiconductor, the AC conductivity can be
40
41 described by the Drude model,^{44, 92-93}
42
43

$$44 \quad \sigma(\omega) = \frac{\sigma_0}{1 + \omega^2 \tau^2} \quad (7)$$

45
46
47 where σ_0 is the DC conductivity, ω is the AC radial frequency, and τ is the relaxation time. This
48
49 model predicts a decrease in conductivity with increases in AC frequency, and hence is not
50
51 consistent with the behavior reported herein.
52
53
54
55
56
57
58
59
60

1
2
3 For charge transport via hopping, isolated hopping sites do not contribute to the DC
4 conductivity. However, as the frequency increases, these isolated hopping sites increasingly
5 contribute to the AC conductivity. The frequency dependence of the conductivity in a wide
6 variety of disordered materials obeys a power law,⁹⁴⁻⁹⁷ and can be written as:
7
8
9

$$\sigma(\omega) = A\omega^s + \sigma_{DC} \quad (8)$$

10
11
12 where A is a constant, ω is the angular frequency, s is the exponent of the angular frequency, and
13 σ_{DC} is the DC conductivity.⁴⁰ The data reported herein are consistent with this model, and a fit
14 of the data to eq 8 yielded $A = 9.94 \times 10^{-17} \text{ S m}^{-1} \text{ s}^{1.95}$, and $s = 1.95$ (**Figure 3**).
15
16
17
18
19
20
21
22

23 *Potential-Dependent Conductivity*

24
25 The potential-dependent conductivity measured by the EC-FET experiments showed only
26 a 1% decrease in conductivity as the potential of the gate was moved positively toward the
27 valence band of the TiO₂. If conduction across the a -TiO₂ relied upon electrons tunneling into
28 the TiO₂ conduction band through a shallow space-charge region at the interface, then the EC-
29 FET experiments would be expected to exhibit a strong dependence of the conductivity on the
30 gate voltage. Specifically, a sharp decrease in conductivity would be observed at potentials
31 positive of the conduction band of the a -TiO₂. The results are thus not consistent with
32 conduction via tunneling of electrons into the conduction band of a -TiO₂.
33
34
35
36
37
38
39
40
41
42

43 The TiO₂ conductivity at positive potentials is sufficient to support faradaic current
44 densities in the range of 10 mA cm⁻² without substantially affecting the OER overpotential. As
45 illustrated in **Figure S6**, for a -TiO₂ conductivities of $\sim 10^{-5} \text{ S cm}$, the potential drop across the
46 p⁺-Si| a -TiO₂|Ni interface is smaller than the potential drop at the a -TiO₂|Ni|electrolyte interface.
47
48
49
50
51
52 The simulation also shows that decreasing conductivity will affect the transport properties across
53 the protecting layer, thus increasing the OER overpotential.
54
55
56
57
58
59
60

C. Conduction across α -TiO₂ Interfaces with Varied Metal Contacts

Contacts between α -TiO₂ and Ti ($\phi = 4.3 \pm 0.2$ eV) or Mg ($\phi = 3.7 \pm 0.2$ eV), which have smaller work functions than that of α -TiO₂ ($\phi = 4.7$ eV) and have mutually similar V_{FB} values, exhibited mutually similar J - V characteristics (**Figure 1**). Contacts between α -TiO₂ and Au ($\phi = 5.1 \pm 0.30$ eV), Pd ($\phi = 5.3 \pm 0.2$ eV), Ir ($\phi = 5.3 \pm 0.2$ eV), or Pt ($\phi = 5.6 \pm 0.07$ eV), which have work functions greater than that of the α -TiO₂, passed ≤ 10 % of the current densities of devices that have low-work-function top contacts. The contact between α -TiO₂ and Ni ($\phi = 5.1 \pm 0.4$ eV) was a notable exception, exhibiting J - V characteristics similar to those with low-work-function metals but with a work function similar to the aforementioned high-work-function contacts. Contacts to low-work-function metals moreover showed less resistance than contacts to high-work-function metals.

Some differences in the J - V behavior among the devices with high-work-function contacts were evident; specifically, at biases < 100 mV, devices with Pd contacts passed only $\sim 10\%$ of the current passed by devices with Au contacts. In decreasing order, devices with Au, Ir, Pt, Pd top contacts exhibited a reduction in current that matched (except for Pd) the order in which the work functions of the metal contacts increase (Au, Pd, Ir, Pt).

The work functions for the various clean metals were measured by UPS under high-vacuum conditions, whereas the conduction was measured for the e-beam deposited metal in contact with the TiO₂ substrate. Polycrystalline metals have multiple crystal faces exposed, so the measurements give an average over the various crystal faces. The averaging is expected to be different depending on the phenomena measured. Also, the fraction of each exposed face may not be the same for the clean metal compared to that of the metal sputtered onto a TiO₂

1
2
3 surface. Thus, only a rough correlation is expected between the work functions measured by UPS
4
5 and the measured J - V behavior.
6

7
8 Space-charge limited current spectroscopy was used to determine the mobility and the
9
10 trap density in the TDMAT α -TiO₂ films. The trap density and mobility were found for Au, Ir, Pt
11
12 and Pd as well as Ir, Pt and Pd, respectively. As can be seen in **Figure 2b** and **Table S2**, the trap
13
14 density and mobility were found to be $1 \times 10^{19} \text{ cm}^{-3}$ and $6.5 \pm 3 \times 10^{-4} \text{ cm}^2 \text{ V}^{-1} \text{ s}^{-1}$, respectively,
15
16 and essentially independent of the top contact. The mobility value was used assumed to be
17
18 independent of the top contact's work function and was thus used to determine the effective
19
20 carrier concentration for all of the top contacts. The effective carrier concentration found using
21
22 this mobility value is in agreement with the carrier concentration observed when measuring the
23
24 carrier concentration by the Hall effect with In contacts (**Figure 2c**). In addition, the mobility
25
26 measured is in agreement with the predicted mobility found by DFT+U methods of $2 \times 10^{-4} \text{ cm}^2$
27
28 $\text{V}^{-1} \text{ s}^{-1}$ by Pham et al.⁴⁷
29
30
31
32

33
34 Devices with a top contact less than $\sim 5.2 \text{ eV}$ showed to have the (effective) free-carrier
35
36 concentration of the device to be independent of the work function. Greater than the $\sim 5.2 \text{ eV}$
37
38 the devices' (effective) free-carrier concentration decreases by $10^1 - 10^2 \text{ cm}^{-3}$ and is dependent on
39
40 the work function. The former devices with contacts to metals that have work functions less than
41
42 the work function of α -TiO₂ had the (effective) free-carrier concentrations on the order of 10^{16}
43
44 cm^{-3} . Conversely, the effective free-carrier concentrations in the α -TiO₂ for devices with contacts
45
46 greater than the work function of α -TiO₂ were $\sim 10^{14} - 10^{15} \text{ cm}^{-3}$, again with the exception of Ni,
47
48 which showed free-carrier concentrations similar to those measured for contacts with the low-
49
50 work-function metals.
51
52
53
54
55
56
57
58
59
60

1
2
3 The dependence on the work function can consistently be ascribed to band-bending in the
4 TiO₂ induced by the respective top contact. Metals with a work function greater than the Fermi-
5 level of the *a*-TiO₂ bend the defect band away from the Fermi level, which will not change the
6 occupancy of the defect band. Conversely, metals with a work function less than the Fermi-level
7 of the *a*-TiO₂ will cause the defect band to bend towards, and even above the Fermi-level. With
8 states above the Fermi-level, mobile charge-carriers (electrons) will empty these states, thus
9 converting Ti³⁺ into Ti⁴⁺.
10
11
12
13
14
15
16
17
18

19 These free-carrier concentrations are an effective average for the *a*-TiO₂, because the
20 depletion width can extend through roughly half the thickness of the film. The conductivity of
21 the *a*-TiO₂ correlates with the Ti³⁺ concentration in the *a*-TiO₂ films, so any local change to the
22 Ti³⁺ concentration will affect the conductivity of the *a*-TiO₂.
23
24
25
26
27

28 Conduction through the defect band can occur by hopping between sites (e.g. Ti⁴⁺/Ti³⁺). If
29 defect sites exist above the Fermi level of the system, then those sites would have fewer free
30 electrons that can hop between sites, and hence conduction is expected to be less favorable in
31 that part of the band.
32
33
34
35
36

37 The *J-V* behavior of the films with different metal contacts is consistent with an
38 equilibration process between the *a*-TiO₂ and the metal contact in conjunction with Fermi level
39 pinning in the TiO₂. During equilibration, low-work-function metals (e.g. Mg, Ti) contacts inject
40 electrons into the *a*-TiO₂, whereas high-work-function contacts extract electrons from the *a*-
41 TiO₂. In this process, most of the electrons would be expected to come from, or enter, the near-
42 surface states of the TiO₂ defect band that are responsible for the Fermi level pinning, thus the
43 number of Ti³⁺ sites close to the surface remain the same or decrease.
44
45
46
47
48
49
50
51
52
53
54
55
56
57
58
59
60

1
2
3 The very low work functions of Mg and Ti suggest that the TiO₂ is forced into
4 accumulation, primarily producing charge mostly on or near the surface, as opposed to
5 substantial band bending. The Ti³⁺ defect sites would thus be available for conduction through
6 the TiO₂. Alternatively, the noble metals, with high work functions, are expected to remove
7 electrons from the near-surface states, and thus reduce the numbers of Ti³⁺ sites close to the
8 surface.^{16, 42} This process would produce bending of the defect band and Ti³⁺ sites at higher
9 energy than the Fermi level would be lost, thus decreasing conduction through that part of the
10 band. The near-surface states would be more affected, resulting in relatively few Ti³⁺ sites on
11 the surface and thus forming a barrier to conduction between the TiO₂ and the metal.
12
13
14
15
16
17
18
19
20
21
22

23
24 Attempts have been made to observe the ‘draining’ of the defect band by both EPR and
25 valence-band spectra. The density of states for any deposited metal would overlap and quickly
26 overpower the Ti³⁺ signal for the valence band spectra, even for <1 nm of deposited metal. The
27 analogous experiment for EPR was attempted using <10 nm of deposited metal. However, the
28 small amount of metal was so strongly absorbing of the incoming microwaves that the
29 instrument could not be tuned to collect the spectrum.
30
31
32
33
34
35
36
37

38 This simple band-bending picture does not fully explain the observations regarding
39 changes in the measured *a*-TiO₂ film conductivity with different metal contacts. The work
40 function of Ni (5.1 ± 0.4 eV) is greater than that of *a*-TiO₂ (4.7 eV) and closer to that of Au (5.1
41 ± 0.3 eV) than to Ti or Mg (≤ 4.3 eV). Furthermore, the data support a wide dispersion in
42 energy (~ 0.8 eV) for the defect band associated with Ti³⁺ states, which would allow a substantial
43 density of defect states to remain below the *a*-TiO₂ Fermi level, for all high-work-function
44 contacts examined herein. However, after subtraction of a Shirley-type background, the defect
45 band peak was fitted with a Gauss-Lorentz peak profile with a 40% Gaussian contribution and
46
47
48
49
50
51
52
53
54
55
56
57
58
59
60

1
2
3 60% Lorentzian contribution. The obtained peak broadening of ~ 0.8 eV can thus be split into the
4
5 0.32 eV instrumental broadening (Gaussian) and 0.48 eV intrinsic lifetime broadening
6
7 (Lorentzian).
8
9

10 Differences in chemical reactivity might also contribute to the observed differences in
11
12 behavior of the metal contacts; specifically, noble metals (Au, Ir, Pt, and Pd) showed lower
13
14 conduction across interfaces with *a*-TiO₂ than non-noble metals (Mg, In, Ti, Ni). Thus, the
15
16 contact interface between the metal and the TiO₂ may also play a role in providing low resistance
17
18 contacts. Ir, an active catalyst of the oxygen-evolution reaction in acidic electrolytes, does not
19
20 form a highly conductive contact to *a*-TiO₂; however, deposition of an acid-stable metal (Ti) that
21
22 does form a highly conductive contact to *a*-TiO₂ prior to deposition of the Ir catalyst allowed
23
24 beneficial integration of the Ir catalyst with the *a*-TiO₂ coating, yielding photoanodes that exhibit
25
26 high fill factors for water oxidation in 1.0 M H₂SO₄(aq).
27
28
29

30
31 In the expected behavior of Ni when comparing its work function to the work function of
32
33 the *a*-TiO₂, it has been shown that the interface is not the source of the discrepancy. The
34
35 Si|TiO₂|Ni|electrolyte interface has been probed via ambient pressure XPS.^{17, 48} It has been
36
37 shown that for ultra-thin layers of Ni (< 1 nm) no conduction was observed in Fe(CN)₆^{3-/4-}(aq)
38
39 and 1.0 M KOH(aq). The conductivity and OER performance was observed and greatly
40
41 increased for $d_{\text{Ni}} > 1$ nm. For thin Ni layers under oxidative conditions, only oxidized Ni phases
42
43 are expected (NiO_x, NiOOH is the catalyst phase, and under the OER conditions at pH 14 no
44
45 metallic Ni can exist). However, small amounts of metallic Ni phases for $d_{\text{Ni}} > 0.6$ nm were
46
47 observed (using AP-XPS under potential control in 1.0 M KOH(aq)) which increased in intensity
48
49 for increased deposition of Ni. This behavior led to the proposed picture of a TiO₂|Ni|NiO_x
50
51 structure under OER, analogous to the structure of a TiO₂|Ti interface.⁴⁸ Separate ex-situ UHV
52
53
54
55
56
57
58
59
60

1
2
3 measurements using different excitation energies and varying the electron emission angle
4
5 confirmed the presence of a metallic Ni phase below the surface. In addition, cross-sectional
6
7 TEM and SEM images of the TiO₂|Ni interface region further support the presence of metallic Ni
8
9 at the interface of the TDMAT *a*-TiO₂.^{4, 18}

10
11
12 The reason for Ni's divergence from the expected behavior is attributed to its work
13
14 function. The work function of Ni although is more positive of the *a*-TiO₂, it is not sufficiently
15
16 positive enough to cause a significant reduction of Ti³⁺ concentration at the interface but rather a
17
18 slight reduction of the concentration at the interface due to the broad width of the Ti³⁺ defect
19
20 band.
21
22
23
24
25

26 V. Conclusions

27
28 *a*-TiO₂ films deposited via ALD contained a broad (~ 0.8 eV) defect band between the
29
30 TiO₂ Fermi level and TiO₂ valence band. For ALD TiO₂ films deposited under varied conditions
31
32 and using varied precursors, the size of the defect band correlated with both the bulk
33
34 conductivity of the *a*-TiO₂ films, and the Ti³⁺ concentration observed via EPR spectroscopy. In
35
36 combination with a variety of solid-state measurements, including temperature-dependent
37
38 conductivity, the data show that conduction through the bulk TiO₂ films is consistent with
39
40 hopping mechanism between Ti³⁺ and adjacent Ti⁴⁺ sites as opposed to conduction via the
41
42 conduction or valence bands. The wide defect band associated with Ti³⁺ sites spans an energy
43
44 level comparable to the valence bands of light-absorbing semiconductors such as Si. Thus,
45
46 allowing anodic conduction across that would otherwise present a ~ 2 eV barrier to anodic
47
48 conduction.
49
50
51
52
53
54
55
56
57
58
59
60

1
2
3 The conduction across interfaces between metal contacts and *a*-TiO₂ films depended on
4 the metal. For the metals examined, interfaces with metals having work functions less than *a*-
5 TiO₂ generally provided higher conductivities than interfaces with metals having work functions
6 greater than *a*-TiO₂. These observations are mostly consistent with a Ti^{3+/4+} conduction that
7 makes use of defect sites close to the surface both to reduce the band bending in the bulk of the
8 TiO₂ and to provide either an insulating or conducting interface between the TiO₂ and the metal.
9 Thus, for metals with low work function, a low resistance path is provided by Ti³⁺ sites, whereas
10 for high work-function metals, the Ti³⁺ sites are depleted and the resistance consequently
11 increases. Ni, while having a relatively high work function, acts like a low work function metal
12 and thus constitutes a notable exception. Properties of the metal contact other than the work
13 function may thus contribute to the different conductivities of interfaces with *a*-TiO₂. The
14 observations provide guidance for a synergistic choice for contacts to *a*-TiO₂ films, showing that
15 improved performance can be obtained for sunlight-driven water-oxidation using an n-Si|*a*-TiO₂
16 photoanode integrated with an Ir catalyst when a Ti interconnect is inserted between the *a*-TiO₂
17 and Ir catalyst relative to the situation in which the Ir catalyst is deposited directly onto the *a*-
18 TiO₂.

19
20
21
22
23
24
25
26
27
28
29
30
31
32
33
34
35
36
37
38
39
40
41
42
43
44
45
46
47
48
49
50
51
52
53
54
55
56
57
58
59
60

ACKNOWLEDGEMENTS

This work was supported through the Office of Science of the U.S. Department of Energy (DOE) under Award No. DE-SC0004993 to the Joint Center for Artificial Photosynthesis, a DOE Energy Innovation Hub. P.D.N. and C.W.R. thank support from the National Science Foundation for graduate research fellowships. C.W.R. also thanks the Link Energy Foundation for a graduate research fellowship. Research was in part carried out at the Molecular Materials Resource Center of the Beckman Institute and at the Microanalysis Center of the California Institute of Technology. D.J.F. acknowledges the financial support by the UK Engineering and Physical Sciences Research Council through the PVTEAM programme (EP/L017792/1). We thank Dr. Y. Guan for secondary-ion mass spectroscopy measurements; Dr. Angelo Di Bilio and Dr. Paul H. Oyala for EPR measurements; and K. Papadantonakis for assistance with editing this manuscript. S.H and S.J.K acknowledge start-up support from the Tomkat Foundation.

AUTHOR INFORMATION

Corresponding Authors

*E-mail: nslewis@caltech.edu (Nathan S. Lewis) shu.hu@yale.edu (Shu Hu)
steven.konezny@yale.edu (Steven J. Konezny)

Notes

The authors declare no competing financial interest.

VI. References

1. Pourbaix, M., *Atlas of Electrochemical Equilibria in Aqueous Solutions*, Second Edition ed.; National Association of Corrosion, 1974.
2. Lewis, N. S., Developing a Scalable Artificial Photosynthesis Technology through Nanomaterials by Design. *Nat. Nanotechnol.* **2016**, *11*, 1010-1019.

- 1
2
3 3. Haussener, S.; Hu, S.; Xiang, C.; Weber, A. Z.; Lewis, N. S., Simulations of the
4 Irradiation and Temperature Dependence of the Efficiency of Tandem Photoelectrochemical
5 Water-Splitting Systems. *Energy Environ. Sci.* **2013**, *6*, 3605.
- 6
7
8 4. Hu, S.; Shaner, M. R.; Beardslee, J. A.; Lichterman, M.; Brunshwig, B. S.; Lewis, N. S.,
9 Amorphous TiO₂ Coatings Stabilize Si, Gaas, and Gap Photoanodes for Efficient Water
10 Oxidation. *Science* **2014**, *344*, 1005-1009.
- 11
12
13 5. Shaner, M. R.; Hu, S.; Sun, K.; Lewis, N. S., Stabilization of Si Microwire Arrays for
14 Solar-Driven H₂O Oxidation to O₂(G) in 1.0 M Koh(Aq) Using Conformal Coatings of
15 Amorphous TiO₂. *Energy Environ. Sci.* **2015**, *8*, 203-207.
- 16
17
18 6. Sun, K.; McDowell, M. T.; Nielander, A. C.; Hu, S.; Shaner, M. R.; Yang, F.;
19 Brunshwig, B. S.; Lewis, N. S., Stable Solar-Driven Water Oxidation to O₂(G) by Ni-Oxide
20 Coated Silicon Photoanodes. *J. Phys. Chem. Lett.* **2015**, *6*, 592-598.
- 21
22
23 7. Chen, Y. W.; Prange, J. D.; Dühnen, S.; Park, Y.; Gunji, M.; Chidsey, C. E. D.;
24 McIntyre, P. C., Atomic Layer-Deposited Tunnel Oxide Stabilizes Silicon Photoanodes for
25 Water Oxidation. *Nat. Mater.* **2011**, *10*, 539-544.
- 26
27
28 8. Kainthla, R. C.; Zelenay, B.; Bockris, J. O. M., Protection of N-Si Photoanode against
29 Photocorrosion in Photoelectrochemical Cell for Water Electrolysis. *J. Electrochem. Soc.* **1986**,
30 *133*, 248-253.
- 31
32
33 9. Kenney, M. J.; Gong, M.; Li, Y.; Wu, J. Z.; Feng, J.; Lanza, M.; Dai, H., High-
34 Performance Silicon Photoanodes Passivated with Ultrathin Nickel Films for Water Oxidation.
35 *Science* **2013**, *342*, 836-840.
- 36
37
38 10. Mei, B.; Seger, B.; Pedersen, T.; Malizia, M.; Hansen, O.; Chorkendorff, I.; Vesborg, P.
39 C. K., Protection of P⁺-N-Si Photoanodes by Sputter-Deposited Ir/IrO_x Thin Films. *J. Phys.*
40 *Chem. Lett.* **2014**, *5*, 1948-1952.
- 41
42
43 11. Yang, J., et al., Efficient and Sustained Photoelectrochemical Water Oxidation by Cobalt
44 Oxide/Silicon Photoanodes with Nanotextured Interfaces. *J. Am. Chem. Soc.* **2014**, *136*, 6191-4.
- 45
46
47 12. Zhou, X.; Liu, R.; Sun, K.; Papadantonakis, K. M.; Brunshwig, B. S.; Lewis, N. S., 570
48 Mv Photovoltage, Stabilized N-Si/CoO_x Heterojunction Photoanodes Fabricated Using Atomic
49 Layer Deposition. *Energy Environ. Sci.* **2016**, *9*, 892-897.
- 50
51
52
53
54
55
56
57
58
59
60

- 1
2
3 13. McDowell, M. T.; Lichterman, M. F.; Spurgeon, J. M.; Hu, S.; Sharp, I. D.; Lewis, N. S.,
4 Improved Stability of Polycrystalline Bismuth Vanadate Photoanodes by Use of Dual-Layer
5 Thin TiO₂/Ni Coatings. *J. Phys. Chem. C* **2014**, *118*, 19618-19624.
6
7
- 8 14. Lichterman, M. F.; Carim, A. I.; McDowell, M. T.; Hu, S.; Gray, H. B.; Brunshwig, B.
9 S.; Lewis, N. S., Stabilization of N-Cadmium Telluride Photoanodes for Water Oxidation to
10 O₂(G) in Aqueous Alkaline Electrolytes Using Amorphous TiO₂ Films Formed by Atomic-Layer
11 Deposition. *Energy Environ. Sci.* **2014**, *7*, 3334-3337.
12
13
- 14 15. Kohl, P. A.; Frank, S. N.; Bard, A. J., Semiconductor Electrodes Xi. Behavior of N- and
15 P-Type Single-Crystal Semiconductors Covered with Thin Normal-TiO₂ Films. *J. Electrochem.*
16 *Soc.* **1977**, *124*, 225-229.
17
18
- 19 16. Hu, S.; Richter, M. H.; Lichterman, M. F.; Beardslee, J.; Mayer, T.; Brunshwig, B. S.;
20 Lewis, N. S., Electrical, Photoelectrochemical, and Photoelectron Spectroscopic Investigation of
21 the Interfacial Transport and Energetics of Amorphous TiO₂/Si Heterojunctions. *J. Phys. Chem.*
22 *C* **2016**, *120*, 3117-3129.
23
24
- 25 17. Lichterman, M. F., et al., Direct Observation of the Energetics at a Semiconductor/Liquid
26 Junction by Operando X-Ray Photoelectron Spectroscopy. *Energy Environ. Sci.* **2015**, *8*, 2409-
27 2416.
28
- 29 18. McDowell, M. T.; Lichterman, M. F.; Carim, A. I.; Liu, R.; Hu, S.; Brunshwig, B. S.;
30 Lewis, N. S., The Influence of Structure and Processing on the Behavior of TiO₂ Protective
31 Layers for Stabilization of N-Si/TiO₂/Ni Photoanodes for Water Oxidation. *ACS Appl. Mater.*
32 *Interfaces* **2015**, *7*, 15189-15199.
33
34
- 35 19. Bae, D.; Shayestehaminzadeh, S.; Thorsteinsson, E. B.; Pedersen, T.; Hansen, O.; Seger,
36 B.; Vesborg, P. C. K.; Ólafsson, S.; Chorkendorff, I., Protection of Si Photocathode Using TiO₂
37 Deposited by High Power Impulse Magnetron Sputtering for H₂ Evolution in Alkaline Media.
38 *Sol. Energy Mater. Sol. Cells* **2016**, *144*, 758- 765.
39
40
- 41 20. Seger, B.; Pedersen, T.; Laursen, A. B.; Vesborg, P. C.; Hansen, O.; Chorkendorff, I.,
42 Using TiO₂ as a Conductive Protective Layer for Photocathodic H₂ Evolution. *J. Am. Chem. Soc.*
43 **2013**, *135*, 1057-1064.
44
45
- 46 21. Seger, B.; Tilley, D. S.; Pedersen, T.; Vesborg, P. C. K.; Hansen, O.; Grätzel, M.;
47 Chorkendorff, I., Silicon Protected with Atomic Layer Deposited TiO₂: Durability Studies of
48 Photocathodic H₂ Evolution. *RSC Adv.* **2013**, *3*, 25902.
49
50
51
52
53
54
55
56
57
58
59
60

- 1
2
3 22. Mei, B.; Pedersen, T.; Malacrida, P.; Bae, D.; Frydendal, R.; Hansen, O.; Vesborg, P. C.;
4 Seger, B.; Chorkendorff, I., Crystalline TiO₂: A Generic and Effective Electron-Conducting
5 Protection Layer for Photoanodes and Cathodes. *J. Phys. Chem. C* **2015**, *119*, 15019-15027.
6
7 23. Li, M.; Hebenstreit, W.; Diebold, U.; Tyryshkin, A. M.; Bowman, M. K.; Dunham, G.
8 G.; Henderson, M. A., The Influence of the Bulk Reduction State on the Surface Structure and
9 Morphology of Rutile TiO₂ (110) Single Crystals. *The Journal of Physical Chemistry B* **2000**,
10 *104*, 4944-4950.
11
12 24. Su, J.; Zou, X.-X.; Zou, Y.-C.; Li, G.-D.; Wang, P.-P.; Chen, J.-S., Porous Titania with
13 Heavily Self-Doped Ti³⁺ for Specific Sensing of Co at Room Temperature. *Inorg Chem* **2013**,
14 *52*, 5924-5930.
15
16 25. Khomenko, V.; Langer, K.; Rager, H.; Fett, A., Electronic Absorption by Ti³⁺ Ions and
17 Electron Delocalization in Synthetic Blue Rutile. *Phys Chem Miner* **1998**, *25*, 338-346.
18
19 26. Amano, F.; Nakata, M.; Yamamoto, A.; Tanaka, T., Effect of Ti³⁺ Ions and Conduction
20 Band Electrons on Photocatalytic and Photoelectrochemical Activity of Rutile Titania for Water
21 Oxidation. *J. Phys. Chem. C* **2016**, *120*, 6467-6474.
22
23 27. Chen, X.; Liu, L.; Peter, Y. Y.; Mao, S. S., Increasing Solar Absorption for
24 Photocatalysis with Black Hydrogenated Titanium Dioxide Nanocrystals. *Science* **2011**, *331*,
25 746-750.
26
27 28. Zuo, F.; Wang, L.; Wu, T.; Zhang, Z.; Borchardt, D.; Feng, P., Self-Doped Ti³⁺
28 Enhanced Photocatalyst for Hydrogen Production under Visible Light. *J. Am. Chem. Soc.* **2010**,
29 *132*, 11856-11857.
30
31 29. Xing, M.; Fang, W.; Nasir, M.; Ma, Y.; Zhang, J.; Anpo, M., Self-Doped Ti³⁺-Enhanced
32 TiO₂ Nanoparticles with a High-Performance Photocatalysis. *J. Catal.* **2013**, *297*, 236-243.
33
34 30. Hoang, S.; Berglund, S. P.; Hahn, N. T.; Bard, A. J.; Mullins, C. B., Enhancing Visible
35 Light Photo-Oxidation of Water with TiO₂ Nanowire Arrays Via Cotreatment with H₂ and NH₃:
36 Synergistic Effects between Ti³⁺ and N. *J. Am. Chem. Soc.* **2012**, *134*, 3659-3662.
37
38 31. Verlage, E.; Hu, S.; Liu, R.; Jones, R. J. R.; Sun, K.; Xiang, C.; Lewis, N. S.; Atwater, H.
39 A., A Monolithically Integrated, Intrinsically Safe, 10% Efficient, Solar-Driven Water-Splitting
40 System Based on Active, Stable Earth-Abundant Electrocatalysts in Conjunction with Tandem
41 Iii-V Light Absorbers Protected by Amorphous TiO₂ Films. *Energy Environ. Sci.* **2015**, *8*, 3166-
42 3172.
43
44
45
46
47
48
49
50
51
52
53
54
55
56
57
58
59
60

- 1
2
3 32. Piercy, B. D.; Losego, M. D., Tree-Based Control Software for Multilevel Sequencing in
4 Thin Film Deposition Applications. *J. Vac. Sci. Technol. B.* **2015**, *33*, 043201.
5
6 33. Plana, D.; Humphrey, J.; Bradley, K.; Celorrio, V.; Fermín, D., Charge Transport across
7 High Surface Area Metal/Diamond Nanostructured Composites. *ACS Appl. Mater. Interfaces*
8 **2013**, *5*, 2985-2990.
9
10 34. Roest, A.; Kelly, J.; Vanmaekelbergh, D.; Meulenkaamp, E., Staircase in the Electron
11 Mobility of a ZnO Quantum Dot Assembly Due to Shell Filling. *Phys. Rev. Lett.* **2002**, *89*,
12 036801.
13
14 35. Olthuis, W.; Streekstra, W.; Bergveld, P., Theoretical and Experimental-Determination of
15 Cell Constants of Planar-Interdigitated Electrolyte Conductivity Sensors. *Sens. Actuators, B*
16 **1995**, *24*, 252-256.
17
18 36. Michaelson, H. B., The Work Function of the Elements and Its Periodicity. *J. Appl. Phys.*
19 **1977**, *48*, 4729-4733.
20
21 37. Hofmann, T.; Yu, T. H.; Folsie, M.; Weinhardt, L.; Bar, M.; Zhang, Y. F.; Merinov, B.
22 V.; Myers, D. J.; Goddard, W. A.; Heske, C., Reply to "Comment on 'Using Photoelectron
23 Spectroscopy and Quantum Mechanics to Determine D-Band Energies of Metals for Catalytic
24 Applications'". *Journal of Physical Chemistry C* **2013**, *117*, 6916-6917.
25
26 38. Hofmann, T.; Yu, T. H.; Folsie, M.; Weinhardt, L.; Bar, M.; Zhang, Y. F.; Merinov, B.
27 V.; Myers, D. J.; Goddard, W. A.; Heske, C., Using Photoelectron Spectroscopy and Quantum
28 Mechanics to Determine D-Band Energies of Metals for Catalytic Applications. *Journal of*
29 *Physical Chemistry C* **2012**, *116*, 24016-24026.
30
31 39. Chiu, F. C., A Review on Conduction Mechanisms in Dielectric Films. *Adv. Mater. Sci.*
32 *Eng.* **2014**.
33
34 40. Bottger, H.; Bryksin, V. V., *Hopping Conduction in Solids*; Akademie-Verlag Berlin,
35 1985.
36
37 41. Rose, A., Space-Charge-Limited Currents in Solids. *Phys. Rev.* **1955**, *97*, 1538.
38
39 42. Tredgold, R. H., *Space Charge Conduction in Solids*; Elsevier Pub. Co., 1966.
40
41 43. Kim, S.; Jeong, H. Y.; Choi, S. Y.; Choi, Y. K., Comprehensive Modeling of Resistive
42 Switching in the Al/TiO_x/TiO₂/Al Heterostructure Based on Space-Charge-Limited Conduction.
43 *Appl. Phys. Lett.* **2010**, *97*.
44
45
46
47
48
49
50
51
52
53
54
55
56
57
58
59
60

- 1
2
3 44. Kao, K.-C.; Hwang, W., *Electrical Transport in Solids: With Particular Reference to*
4 *Organic Semiconductors*
5
6 , 1st ed.; Pergamon Press: Oxford ; New York, 1981.
7
8 45. Riviere, J., Work Function: Measurements and Results. In *Solid State Surface Science*,
9 Green, M., Ed. Decker: New York, 1969; Vol. 1, pp 179–289.
10
11 46. Hölzl, J.; Schulte, F. K., Work Function of Metals. In *Solid Surface Physics*, Höhler, G.,
12 Ed. Springer-Verlag: Berlin, 1979; pp 1-150.
13
14 47. Pham, H. H.; Wang, L. W., Oxygen Vacancy and Hole Conduction in Amorphous TiO₂.
15 *Phys. Chem. Chem. Phys.* **2015**, *17*, 541-550.
16
17 48. Lichterman, M. F., et al., An Electrochemical, Microtopographical and Ambient Pressure
18 X-Ray Photoelectron Spectroscopic Investigation of Si/TiO₂/Ni/Electrolyte Interfaces. *J.*
19 *Electrochem. Soc.* **2016**, *163*, H139 - H146.
20
21 49. Niilisk, A.; Moppel, M.; Pärs, M.; Sildos, I.; Jantson, T.; Avarmaa, T.; Jaaniso, R.; Aarik,
22 J., Structural Study of TiO₂ Thin Films by Micro-Raman Spectroscopy. *Open Physics* **2006**, *4*,
23 105-116.
24
25 50. Piercy, B. D.; Leng, C. Z.; Losego, M. D., Variation in the Density, Optical
26 Polarizabilities, and Crystallinity of TiO₂ Thin Films Deposited Via Atomic Layer Deposition
27 from 38 to 150° C Using the Titanium Tetrachloride-Water Reaction. *J. Vac. Sci. Technol., A*
28 **2017**, *35*, 03E107.
29
30 51. Suriye, K.; Jongsomjit, B.; Satayaprasert, C.; Praserthdam, P., Surface Defect (Ti³⁺)
31 Controlling in the First Step on the Anatase TiO₂ Nanocrystal by Using Sol-Gel Technique. *Appl.*
32 *Surf. Sci.* **2008**, *255*, 2759-2766.
33
34 52. Suriye, K.; Praserthdam, P.; Jongsomjit, B., Impact of Ti³⁺ Present in Titania on
35 Characteristics and Catalytic Properties of the Co/TiO₂ Catalyst. *Ind. Eng. Chem. Res.* **2005**, *44*,
36 6599-6604.
37
38 53. Howe, R. F.; Gratzel, M., Epr Observation of Trapped Electrons in Colloidal Titanium
39 Dioxide. *J. Phys. Chem.* **1985**, *89*, 4495-4499.
40
41 54. Hoang, S.; Berglund, S. P.; Hahn, N. T.; Bard, A. J.; Mullins, C. B., Enhancing Visible
42 Light Photo-Oxidation of Water with TiO₂ Nanowire Arrays Via Cotreatment with H₂ and NH₃:
43 Synergistic Effects between Ti³⁺ and N. *J. Am. Chem. Soc.* **2012**, *134*, 3659-3662.
44
45
46
47
48
49
50
51
52
53
54
55
56
57
58
59
60

- 1
2
3 55. Reddy, S. L.; Reddy, G. S.; Endo, T., *Electronic (Absorption) Spectra of 3d Transition*
4 *Metal Complexes*; INTECH, 2012.
- 5
6 56. Fu, G.; Zhou, P.; Zhao, M. M.; Zhu, W. D.; Yan, S. C.; Yu, T.; Zou, Z. G., Carbon
7 Coating Stabilized Ti³⁺-Doped TiO₂ for Photocatalytic Hydrogen Generation under Visible Light
8 Irradiation. *Dalton Trans.* **2015**, *44*, 12812-12817.
- 9
10 57. Liu, H.; Ma, H.; Li, X.; Li, W.; Wu, M.; Bao, X., The Enhancement of TiO₂
11 Photocatalytic Activity by Hydrogen Thermal Treatment. *Chemosphere* **2003**, *50*, 39-46.
- 12
13 58. Yildiz, A.; Iacomi, F.; Mardare, D., Polaron Transport in TiO₂ Thin Films. *J. Appl. Phys.*
14 **2010**, *108*, 083701.
- 15
16 59. Wendt, S.; Sprunger, P. T.; Lira, E.; Madsen, G. K.; Li, Z.; Hansen, J. Ø.; Matthiesen, J.;
17 Blekinge-Rasmussen, A.; Lægsgaard, E.; Hammer, B., The Role of Interstitial Sites in the Ti3d
18 Defect State in the Band Gap of Titania. *Science* **2008**, *320*, 1755-1759.
- 19
20 60. Schierbaum, K.-D.; Fischer, S.; Wincott, P.; Hardman, P.; Dhanak, V.; Jones, G.;
21 Thornton, G., Electronic Structure of Pt Overlayers on (1×3) Reconstructed TiO₂ (100) Surfaces.
22 *Surf. Sci.* **1997**, *391*, 196-203.
- 23
24 61. Linderälv, C.; Lindman, A.; Erhart, P., A Unifying Perspective on Oxygen Vacancies in
25 Wide Band Gap Oxides. *J. Phys. Chem. Lett.* **2018**, *9*, 222-228.
- 26
27 62. Henkel, K.; Das, C.; Kot, M.; Schmeißer, D.; Naumann, F.; Kärkkäinen, I.; Gargouri, H.,
28 In-Gap States in Titanium Dioxide and Oxynitride Atomic Layer Deposited Films. *J. Vac. Sci.*
29 *Technol., A* **2017**, *35*, 01B135.
- 30
31 63. Das, C.; Richter, M.; Tallarida, M.; Schmeißer, D., Electronic Properties of Atomic Layer
32 Deposition Films, Anatase and Rutile TiO₂ Studied by Resonant Photoemission Spectroscopy. *J.*
33 *Phys. D: Appl. Phys.* **2016**, *49*, 275304.
- 34
35 64. Park, S.-J.; Lee, J.-P.; Jang, J. S.; Rhu, H.; Yu, H.; You, B. Y.; Kim, C. S.; Kim, K. J.;
36 Cho, Y. J.; Baik, S., In Situ Control of Oxygen Vacancies in TiO₂ by Atomic Layer Deposition
37 for Resistive Switching Devices. *Nanotechnology* **2013**, *24*, 295202.
- 38
39 65. Zhang, Y.; Ding, Z.; Foster, C. W.; Banks, C. E.; Qiu, X.; Ji, X., Oxygen Vacancies
40 Evoked Blue TiO₂ (B) Nanobelts with Efficiency Enhancement in Sodium Storage Behaviors.
41 *Adv. Funct. Mater.* **2017**, *27*, 1700856.
- 42
43 66. Di Valentin, C.; Pacchioni, G.; Selloni, A., Reduced and N-Type Doped TiO₂: Nature of
44 Ti³⁺ Species. *J. Phys. Chem. C* **2009**, *113*, 20543-20552.
- 45
46
47
48
49
50
51
52
53
54
55
56
57
58
59
60

- 1
2
3 67. Deskins, N. A.; Dupuis, M., Intrinsic Hole Migration Rates in TiO_2 from Density
4 Functional Theory. *J. Phys. Chem. C* **2009**, *113*, 346 - 358.
5
6 68. Deskins, N. A.; Rousseau, R.; Dupuis, M., Localized Electronic States from Surface
7 Hydroxyls and Polarons in TiO_2 (110). *J. Phys. Chem. C* **2009**, *113*, 14583-14586.
8
9 69. Deskins, N. A.; Rousseau, R.; Dupuis, M., Distribution of Ti^{3+} Surface Sites in Reduced
10 TiO_2 . *J. Phys. Chem. C* **2011**, *115*, 7562-7572.
11
12 70. Deskins, N. A.; Rousseau, R.; Dupuis, M., Defining the Role of Excess Electrons in the
13 Surface Chemistry of TiO_2 . *J. Phys. Chem. C* **2010**, *114*, 5891 - 5897.
14
15 71. Zhang, Y.; Ding, Z.; Foster, C. W.; Banks, C. E.; Qiu, X.; Ji, X., Oxygen Vacancies
16 Evoked Blue TiO_2 (B) Nanobelts with Efficiency Enhancement in Sodium Storage Behaviors.
17 *Adv. Funct. Mater.* **2017**, *27*, 1700856.
18
19 72. Pham, H. H.; Wang, L.-W., Oxygen Vacancy and Hole Conduction in Amorphous TiO_2 .
20 *Phys. Chem. Chem. Phys.* **2015**, *17*, 541-550.
21
22 73. Xia, T.; Zhang, Y.; Murowchick, J.; Chen, X., Vacuum-Treated Titanium Dioxide
23 Nanocrystals: Optical Properties, Surface Disorder, Oxygen Vacancy, and Photocatalytic
24 Activities. *Catal Today* **2014**, *225*, 2-9.
25
26 74. Morgan, B. J.; Watson, G. W., Intrinsic N-Type Defect Formation in TiO_2 : A
27 Comparison of Rutile and Anatase from GGA+U Calculations. *J. Phys. Chem. C* **2010**, *114*,
28 2321-2328.
29
30 75. Deskins, N. A.; Dupuis, M., Electron Transport Via Polaron Hopping in Bulk TiO_2 : A
31 Density Functional Theory Characterization. *Phys Rev B* **2007**, *75*.
32
33 76. Nakamura, I.; Negishi, N.; Kutsuna, S.; Ihara, T.; Sugihara, S.; Takeuchi, K., Role of
34 Oxygen Vacancy in the Plasma-Treated TiO_2 Photocatalyst with Visible Light Activity for NO
35 Removal. *J. Mol. Catal. A: Chem.* **2000**, *161*, 205-212.
36
37 77. Diebold, U., The Surface Science of Titanium Dioxide. *Surf. Sci. Rep.* **2003**, *48*, 53-229.
38
39 78. Fukui, K.-i.; Onishi, H.; Iwasawa, Y., Atom-Resolved Image of the TiO_2 (110) Surface
40 by Noncontact Atomic Force Microscopy. *Phys. Rev. Lett.* **1997**, *79*, 4202.
41
42 79. Jin, C.; Liu, B.; Lei, Z.; Sun, J., Structure and Photoluminescence of the TiO_2 Films
43 Grown by Atomic Layer Deposition Using Tetrakis-Dimethylamino Titanium and Ozone.
44 *Nanoscale research letters* **2015**, *10*, 95.
45
46
47
48
49
50
51
52
53
54
55
56
57
58
59
60

- 1
2
3 80. Saha, D.; Ajimsha, R.; Rajiv, K.; Mukherjee, C.; Gupta, M.; Misra, P.; Kukreja, L.,
4 Spectroscopic Ellipsometry Characterization of Amorphous and Crystalline TiO₂ Thin Films
5 Grown by Atomic Layer Deposition at Different Temperatures. *Appl. Surf. Sci.* **2014**, *315*, 116-
6 123.
7
8
9
10 81. Hashimoto, S.; Tanaka, A., Alteration of Ti 2p Xps Spectrum for Titanium Oxide by
11 Low-Energy Ar Ion Bombardment. *Surf. Interface Anal.* **2002**, *34*, 262-265.
12
13 82. Mott, N., Electrons in Non-Crystalline Materials: The Last Twenty Five Years. *Contemp.*
14 *Phys.* **1985**, *26*, 203.
15
16 83. Brunshwig, B. S.; Sutin, N., Energy Surfaces, Reorganization Energies, and Coupling
17 Elements in Electron Transfer. *Coordin Chem Rev* **1999**, *187*, 233-254.
18
19 84. Austin, I. G.; Mott, N. F., Polarons in Crystalline and Non-Crystalline Materials. *Adv.*
20 *Phys.* **2001**, *50*, 757-812.
21
22 85. Yildiz, A.; Lisesivdin, S.; Kasap, M.; Mardare, D., Electrical Properties of TiO₂ Thin
23 Films
24 . *J. Non-Cryst. Solids* **2008**, *354*, 4944-4947.
25
26
27 86. Austin, I. G.; Mott, N. F., Polarons in Crystalline and Non-Crystalline Materials. *Adv.*
28 *Phys.* **1969**, *18*.
29
30 87. Liu, T.; Dupuis, M.; Li, C., Band Structure Engineering: Insights from Defects, Band
31 Gap, and Electron Mobility, from Study of Magnesium Tantalate. *J. Phys. Chem. C* **2016**, *120*,
32 6930 - 6937.
33
34 88. Ju, Y.; Wang, M.; Wang, Y.; Wang, S.; Fu, C., Electrical Properties of Amorphous
35 Titanium Oxide Thin Films for Bolometric Application. *Adv. Condens. Matter Phys.* **2013**, *2013*,
36 1 - 5.
37
38 89. Rao, M. V. R.; Gandhi, Y.; Rao, L. S.; Sahayabaskaran, G.; Veeraiyah, N., Electrical and
39 Spectroscopic Properties of LiF–Bi₂O₃–P₂O₅:TiO₂ Glass System. *Mater. Chem. Phys.* **2011**, *126*,
40 58 - 68.
41
42 90. Sugiyama, K.; Takeuchi, Y., The Crystal Structure of Rutile as a Function of
43 Temperature up to 1600° C. *Z. Kristallogr. Cryst. Mater.* **1991**, *194*, 305-313.
44
45 91. Howard, C. J.; Sabine, T. M.; Dickson, F., Structural and Thermal Parameters for Rutile
46 and Anatase. *Acta Crystallogr. Sec. B* **1991**, *47*, 462-468.
47
48
49
50
51
52
53
54
55
56
57
58
59
60

- 1
2
3 92. Ihle, D.; Lorenz, B., Small-Polaron Conduction and Short-Range Order in Fe₃O₄. *J. Phys.*
4 *C: Solid State Phys.* **1986**, *19*, 5239-5251.
5
6 93. Mott, N. F.; Davis, E. A., *Electronic Processes in Non-Crystalline Materials*, 2nd ed.;
7 Clarendon Press: Oxford,, 1979.
8
9 94. Jonscher, A. K., Universal Dielectric Response. *Nature* **1977**, *267*, 673-679.
10
11 95. Long, A. R., Frequency-Dependent Loss in Amorphous-Semiconductors. *Adv. Phys.*
12 **1982**, *31*, 553-637.
13
14 96. Konezny, S. J.; Richter, C.; Snoeberger, R. C.; Parent, A. R.; Brudvig, G. W.;
15 Schmuttenmaer, C. A.; Batista, V. S., Fluctuation-Induced Tunneling Conductivity in
16 Nanoporous Tio₂ Thin Films. *J. Phys. Chem. Lett.* **2011**, *2*, 1931-1936.
17
18 97. Elliott, S. R., Ac Conduction in Amorphous-Chalcogenide and Pnictide Semiconductors.
19 *Adv. Phys.* **1987**, *36*, 135-218.
20
21
22
23
24
25
26
27
28
29
30
31
32
33
34
35
36
37
38
39
40
41
42
43
44
45
46
47
48
49
50
51
52
53
54
55
56
57
58
59
60